

UNIVERSITY OF HAWAII LIBRARY

**TSUNAMI FORECAST USING AN ADAPTIVE INVERSE ALGORITHM  
FOR THE CHILE-PERU SOURCE REGION**

**A THESIS SUBMITTED TO THE GRADUATE DIVISION  
OF THE UNIVERSITY OF HAWAI'I IN PARTIAL FULFILLMENT  
OF THE REQUIREMENTS FOR THE DEGREE OF**

**MASTER OF SCIENCE**

**IN**

**OCEAN AND RESOURCES ENGINEERING**

**DECEMBER 2006**

**BY**

**Alejandro Sánchez**

**Thesis Committee:**

**Kwok Fai Cheung, Chairperson  
Geno Pawlak  
Ian Robertson**

We certify that we have read this thesis and that, in our opinion, it is satisfactory in scope and quality as a thesis for the degree of Master of Science in Ocean and Resources Engineering.

THESIS COMMITTEE

  
Chairperson





## ACKNOWLEDGEMENTS

I would like to sincerely thank my advisor Dr. Kwok Fai Cheung for his guidance and supervision during this work. I thank Dr. Geno Pawlak for the technical discussions and Dr. Ian Robertson for the useful comments. I want to give special thanks to Sophie Munger for her valuable comments, reviews, and discussions during all of this work. I am grateful to all the Ocean and Resources Engineering students who contributed to this work by providing valuable comments and suggestions, specifically Dr. Yong Wei, Yoshiki Yamazaki, Volker Roëber, and Megan Craw. I also want to state my appreciation to Ms. Edith Katada for her time and expertise in processing all the paperwork.

Financial support in the form of a graduate research assistantship was provided by the National Tsunami Hazard Mitigation Program via Hawai'i State Civil Defense.

## ABSTRACT

The inverse method provides tsunami forecasts based on a regression analysis of near-field water-level data against a database of pre-computed tsunami waveforms corresponding unit slip of predefined subfaults. This thesis describes an improvement to this conventional inverse method by resolving the time sequence of tsunamigenic earthquake events. This adaptive approach provides additional degrees of freedom in the regression analysis to compensate for the errors in the user-specified earthquake time or the lag time in tsunami generation, and most importantly, to account for propagation of earthquake rupture. The algorithm also determines the initial subfaults for the regression analysis based on the arrival times of tsunami waves at water-level stations and those of the pre-computed waveforms. A hindcast analysis for the 1960 Valdivia-Chile, 1995 Antofagasta-Chile, and 2001 Atico-Peru tsunamis demonstrates the capability of the adaptive inverse method. The source parameters and subfault distribution for the Peru-Chile source region are based on seismotectonics and historical earthquakes. The present method produces better results in comparison to the conventional approach and indicates an apparent delay between the generation of the tsunamis and the reported earthquake times for all three events. The results suggest that the slip distribution and earthquake rupture propagation are very important for the near-field results while the bathymetry is the dominant factor which controls the shape of the waveforms in the far-field.

# TABLE OF CONTENTS

List of Tables .....	iii
List of Figures .....	iv
Chapter 1: Introduction .....	1
Chapter 2: Tsunami Source .....	3
2.1 Tsunamigenic Earthquakes .....	3
2.2 Seismotectonics .....	5
2.3 Source Parameters .....	8
2.4 Subfault Distribution .....	10
Chapter 3: Inversion Method .....	11
3.1 Mareogram Database .....	11
3.2 Adaptive Inverse Algorithm .....	12
Chapter 4: Results and Discussion .....	18
4.1 1960 Valdivia-Chile Tsunami .....	18
4.2 1995 Antofagasta-Chile Tsunami .....	20
4.3 2001 Atico-Peru Tsunami .....	22
Chapter 6: Conclusions and Recommendations .....	24

## LIST OF TABLES

<b><u>Table</u></b>		<b><u>Page</u></b>
1.	Source parameters for major tsunamigenic earthquakes ( $M \geq 7.5$ ) in the Peru-Chile subduction zone in the last 100 years.	26
2.	Comparison of slip distributions obtained from the conventional and adaptive inverse methods.	28

## LIST OF FIGURES

<b><u>Figure</u></b>	<b><u>Page</u></b>
1. Definition sketch of a finite rectangular fault model.	29
2. Schematic of a typical cross-section of the Peru-Chile subduction zone.	30
3. Comparison of source parameters of the Peru-Chile subduction zone.	31
4. Tectonic setting and approximate fault areas of major earthquakes in the Chile-Peru subduction zone.	32
5. Subfault distribution for the Peru-Chile subduction zone.	33
6. Computational grid system and water-level stations used in the inverse analysis	34
7. Convergence of the adaptive inverse method for the 1960 Valdivia-Chile tsunami.	35
8. Mareograms and computed waveforms at near-field tide gauges for the 1960 Valdivia-tsunami.	36
9. Computed and recorded waveforms at near-field tide gauges for the 1960 Valdivia-Chile tsunami.	36
10. Computed and recorded waveforms at far-field tide gauges for the 1960 Valdivia-Chile tsunami.	37
11. Convergence of the AIM for the 1995 Antofagasta-Chile tsunami.	38
12. Computed and recorded waveforms at near-field tide gauges for the 1995 Antofagasta-Chile tsunami.	39
13. Computed and recorded waveforms at far-field tide gauges for the 1960 Valdivia-Chile tsunami.	40
14. Convergence of the AIM for the 2001 Atico-Peru tsunami.	41
15. Computed and recorded waveforms at near-field tide gauges for the 2001 Atico Peru tsunami.	42
16. Computed and recorded waveforms at far-field tide gauges for the 2001 Atico Peru tsunami.	43

# CHAPTER 1

## INTRODUCTION

The capability to quantitatively forecast tsunami wave heights at locations far away from the source is crucial for issuance or cancellation of tsunami warnings. Large trans-oceanic tsunamis are generally caused by seismic activity along subduction zones. The Pacific Tsunami Warning Center and the West Coast and Alaska Tsunami Warning Center provide tsunami warnings for most of the countries in and around the Pacific Ocean. The initial tsunami warning is based only on the earthquake magnitude and location. Once the warning is issued, tide gauges, and deep-ocean pressure sensors are monitored for tsunamis. In particular, deep-ocean pressure sensors deployed near the source regions are especially useful because they can provide clear signals of tsunamis away from the shore (Eble and González, 1991; and Hino *et al.*, 2001).

Geophysicists have used tsunami signals recorded by tide gauges to reconstruct seismic events (e.g., Satake, 1987; 1989). In this inverse method, the source region is divided into subfaults with predetermined source parameters and a linear long-wave model is used to generate a database of tsunami waveforms for unit slip of the subfaults. A regression analysis of the tide gauge data with the pre-computed waveforms determines the slip distribution. Johnson (1999) provided a comprehensive review and analysis of this method and showed that the use of tsunami data in an inverse analysis produces comparable results with those obtained using seismic and geodetic data. Titov *et al.* (1999) contemplated the use of the inverse approach to determine the initial conditions for real-time forecasts of trans-Pacific tsunamis.

Wei *et al.* (2001, 2003) extended the inverse method by using the computed slip distribution to forecast or hindcast the tsunami waveforms away from the source. Based on the subfault distribution and source parameters of Johnson (1999) for the Alaska-Aleutian source region, they were able to determine the slip distributions and tsunami

heights in Hawai'i for the 1964 Prince William Sound and 1996 Andreanov tsunami events. Yamazaki *et al.* (2006) subsequently implemented the method for the Japan-Kuril-Kamchatka source region and obtained encouraging results at water-level stations across the Pacific Basin for the 1944 Tonakai and the 1994 Kuril earthquakes. Titov *et al.* (2005) discussed the implementation of the inverse method with deep-ocean pressure sensors to provide Pacific-wide tsunami forecast. Wei (2006) combined the inverse method with real-time simulation to provide tsunami inundation forecasts.

The aforementioned inverse method, which assumes all subfaults to move simultaneously at the user-specified earthquake time, might not fully describe earthquakes with large fault areas. A good example is the 2004 Sumatra-Andaman earthquake, in which the rupture propagated 1,200-1,300 km over a 10 min period (Ammon *et al.*, 2005). This study develops an adaptive inverse algorithm, which determines the timing and rupture sequence of pre-determined subfaults to best-fit recorded tsunami signals. The added versatility of the adaptive scheme is demonstrated through the 1960 Valdivia-Chile, 1995 Antofagasta-Chile, and 2001 Atico-Peru tsunamis. This study focuses on the Peru-Chile source region and complements the work of Wei *et al.* (2001, 2003) and Yamazaki *et al.* (2006) by providing tsunami forecast capabilities for the three source regions that pose the highest risk to the Hawaiian Islands.

## CHAPTER 2

### TSUNAMI SOURCE

#### 2.1 Tsunamigenic Earthquakes

In the South American subduction zone, the Nazca Plate subducts underneath the South American Plate at a rate of 75-80 mm/yr (DeMets *et al.*, 1994). This is a relatively young subduction zone in which there is a strong seismic coupling between the oceanic and continental lithospheres (Kanamori, 1977). The first reports of tsunamis were made by Spanish settlers in the 16<sup>th</sup> century, while some Peruvian legends also describe ancient catastrophes that can be attributed to tsunamis. Berninghausen (1962) reported 49 tsunamis originated from the west coast of South America between 1562 and 1960. The results were subsequently included in the compilation of historic tsunami records for South America by Lomnitz (1970), Soloviev and Go (1975), and Lockridge (1985).

The deformation of the earth surface due to internal faulting is generally described by the elastic theory of dislocation, in which the earth is treated as a homogeneous, isotropic, and elastic material (Steketee, 1958; Okada, 1985). The finite rectangular uniform slip model by Okada (1985) provides the seafloor deformation in terms of the strike, dip, rake, slip, reference depth, and fault length and width (see Appendix A). Figure 1 shows a schematic of the fault model geometry. The strike is the azimuth of the intersection of the fault plane with the horizontal plane. The reference depth is the upper limit of the fault and is always smaller than the focal depth. The dip is the maximum angle between the horizontal plane and the fault plane. The rake angle indicates the direction of the hanging wall block and the slip is the amount of displacement in the rake direction. The resulting surface deformation includes uplift, subsidence, and offset. The surface deformation decreases as the depth of the rupture increases.

Table 1 compiles from previous studies the source parameters of large historical tsunamigenic earthquakes ( $M \geq 7.5$ ) in the Peru-Chile subduction zone during the last 100

years. The events are arranged by latitude and divided into sub-regions. The upper latitude source region is delineated by a large seismic gap between 0 to 9°S, in which no great earthquakes have occurred in the last 400 years and hence is not likely characterized by large thrust-type plate motions (Kelleher, 1972). The southern limit of the source region is delimited at 46°S by a region of very low seismicity with only a few events in the magnitude range 4.5 to 6 (McCann *et al.*, 1979). This study covers the Peru-Chile source from 9 to 46°S. The earthquake characteristics from different sources are listed to provide an estimated range of the values. Prior to the 1922 Atacama event, only the fault type is available, but not the source parameters.

These tsunamigenic earthquakes can be classified into interplate-thrust and intraplate-normal events as illustrated in Figure 2. The dots and circles indicate locations of seismic activities. The arrows on the circles indicate compressive or tensile forces. Typical interplate thrust or reverse earthquakes have shallow depths of less than 50 km and rupture mainly offshore in the direction of the relative plate motion (Stauder, 1973). Some examples in the past century are the 1906 Valparaiso, 1922 Atacama, 1960 Valdivia, and 2001 Atico events listed in Table 1. In an interplate earthquake, an uplift zone is produced by the relative seaward displacement of the overthrusting continental plate along the dipping plane, and an adjacent zone of subsidence is caused by the elastic response of the crust behind the fault block. Because of their location, depth and potential size, thrust earthquakes are considered an important tsunamigenic sources.

There are two types of intraplate-normal events. Outer-rise earthquakes are produced by bending of the oceanic plate prior to subduction and have not produced significant tsunamis in this subduction zone. Slab earthquakes occur due to unbending and thermal stresses at intermediate depths and down-dip tensile forces at greater depths. Between bending in the outer-rise and unbending at intermediate depths, the slab is usually in low stress, which may make the occurrence of large intraslab earthquakes scarce (Seno, 2004). Typical intra-plate normal earthquakes occur at intermediate depths of 35-70 km

below the continent (Choy and Kirby, 2004). In Peru, these activities typically occur along a coastal-plate interior zone located 50 km inland and 30 km deeper than the interplate thrust zone (Dewey and Spence, 1979). A good example of a large non-tsunamigenic normal earthquake is the 1939  $M_w$  8.0 intra-plate event beneath Central Chile (Beck *et al.*, 1998). Although the earthquake was very destructive and killed more than 200 people as reported by Lomnitz (1970), it did not produce a tsunami. The 1970 Peru event is the only tsunami generated by a normal fault mechanism with moment magnitude greater than 7.5, but did not produce a significant trans-Pacific tsunami.

In Summary, intraplate normal events can produce significant local tsunamis, but trans-Pacific tsunamis are typically generated by large interplate-thrust earthquakes. It is therefore reasonable to select the interplate-thrust type earthquakes to define the fault parameters for future trans-Pacific tsunamis that may be generated in the Peru-Chile subduction zone.

### 2.3 Seismotectonics

In addition to the historical events, a review of the seismotectonics is needed to estimate and validate the source parameters. The dip angle of the initial subduction of the oceanic plate can be obtained from bathymetry and seismic reflection and refraction data. For deeper, more landward portions of the subduction, the plate geometry is generally obtained from Wadati-Benioff earthquakes, intermediate magnitude thrust earthquakes, and large thrust earthquakes and their aftershocks. Wadati-Benioff earthquakes occur mainly in the upper oceanic mantle and their distribution can be used to estimate the upper boundary of the subducting plate.

By using earthquakes of magnitude 5 or greater, Isacks and Molnar (1971) calculated a dip of 10 to 15° for the oceanic lithosphere beneath central Peru from 9 to 15°S. Stauder (1975) reported a dip angle of 10 to 15° and a strike angle of 330° for Northern and Central Peru and a strike angle of 300 to 310° for Southern Peru. Barazangi and Isacks

(1976) and Hasegawa and Sacks (1981) reported that the segment of oceanic lithosphere for Central Peru dips from 10 to 30° to a depth of 100 km. The region of Southern Peru between 15 and 18°S is characterized by shallow thrust earthquakes with fault planes dipping east-northeast such as the 1942, 1996 and 2001 earthquakes.

The northern region of Chile between 18 to 23°S is a seismic gap with no earthquakes occurring since 1877 (Chlieh *et al.*, 2004). Delouis (1996) reported on the seismic gap between 22 and 23°S and found that the interplate thrust earthquakes in this region have low-angle dip of 17 to 18°, a strike of 345 to 350° oriented with the trench axis, slip vectors in concord with the direction of convergence, and depths of up to 50 km. Comte *et al.* (1999) calculated an average dip angle of 20° for Northern Chile between 25 and 55 km in depth.

Araujo and Suárez (1994) calculated the geometry of the subducting Nazca plate for the region between 21 and 33°S. They found an initial dip angle of approximately 15° down to a 70 km depth for the whole region and suggested that the initial dip of the subduction zone is independent of the subducting plate geometry at greater depth. Pardo *et al.* (2002b) found an interplate geometry that initially dips at about 10° and gradually increases to 25° at a depth of 45 km for Central Chile between 26 and 35°S. They found that the dip is uniform along the trench axis even across bathymetric features such as the Juan Fernandez Ridge and suggested that the shape of the initial subducting plate is only a function of the characteristics of the interplate collision and is independent of plate age or convergence rate. The significant changes in dip at approximately 45 km deep along Central Chile found by Pardo (2002b) also correlates well with the down-dip limits found by Oleskevich *et al.* (1999) and Tichelaar and Ruff (1991).

The crustal structure of Southern Chile was described by Fisher and Raitt (1962). This section of the trench is intersected by several fracture zones, where the Nazca plate subducts underneath Southern Chile at a shallow angle. The Wadati-Benioff zone is only delineated well enough to infer the dip of subducting slab in the Arauco Peninsula located

at approximately 37.2°S. The dip of the shallow slab beneath this region is approximately 10 to 15° at a depth of 40 km and then increases to 30° at a depth of 125 km (Cifuentes, 1989; Bohm *et al.*, 2002; Lüth *et al.*, 2003). South of the Arauco Peninsula, the dip angle is not very well constrained.

Subduction zones are inherently segmented due to discontinuities in the oceanic lithosphere such as ridges and preexisting faults as well as changes in the continental morphology (Swift and Carr, 1974). These discontinuities can be apparent in the variation of source parameters and provide natural boundaries for earthquake rupture areas by decoupling adjacent segments or interrupting the propagation of earthquake rupture. Therefore, the segmentation of the subduction zone can be obtained from the rupture areas of large historical earthquakes and variations in the source parameters.

The down-dip and up-dip limits of large subducting earthquakes are controlled by various geological and physical factors including the plate age, temperature, composition, and the Moho depth (Hyndman and Wang, 1993). Oleskevich *et al.* (1999) used finite element models to examine the thermal and structural constraints on the up-dip and down-dip limits of great subduction zone earthquakes. The up-dip limit corresponds to the position where the temperature reaches 100°C, which corresponds to a depth of 2-10 km. The down-dip limit corresponds to the depth where the temperature reaches 350° to 450° C or the intersection of the oceanic crust and the bottom limit of the continental crust at approximately 40 km depth. This confirms the findings of Tichelaar and Ruff (1991), who used relocated earthquake hypocenters to estimate the down-dip limit and found that North of 28°S, the seismic coupling extends to a depth of 36 to 41 km, while South of this latitude, under the flat slab region of Chile, the seismic coupling extends to 48-53 km.

## 2.4 Source Parameters

The tectonic structure of the Peru-Chile subduction zone varies significantly along the trench axis, but perpendicular to the trench, the dip of the rupture areas of tsunamigenic earthquakes do not change significantly (Tichelaar and Ruff, 1991). Consequently, a single row of planar faults can be used along the trench axis and the source parameters may be calculated as a function of latitude. The seismotectonics and historical events show that the strike of the faults is approximately parallel to the trench axis. This simplifies the source parameters and the layout of the subfaults. The dip for each sub-region in Table 1 is inferred from seismotectonic studies and taking into consideration historical events. The reference depth is calculated from geometry using the dip angle and the distance between subfaults and the trench axis.

The relative motion between the continental and oceanic plates is divided into thrust earthquakes, stable sliding or aseismic subduction, permanent crustal shortening, and coastal forearc sliver. Coastal forearc sliver is the strike-slip motion of the coastal forearc parallel to the trench and is found in regions where the plate convergence is oblique. This motion causes the earthquake slip vectors at the trench to rotate from the convergence direction toward the trench-normal direction. Despite the significant oblique convergence in the Peru subduction zone, Norabuena *et al.* (1998) found that there is little coastal forearc sliver and slip partitioning. Given the scatter in the rake angle of historical events and the evidence of little slip partitioning in the Peru subduction zone, the earthquake slip vectors are assumed to be in the opposite direction of the relative plate convergence. The direction of plate motion is obtained from the global plate motion model NUVEL-1A (DeMets *et al.*, 1990, 1994).

Figure 3 compares the calculated source parameters along the subduction zone with those listed in Table 1 for tsunamigenic earthquakes with magnitude of 7.5 or greater from circa 1900. The historical events shown with bars represent the range of values found in literature. The source parameters used by NOAA PMEL and developed at the

NOAA Center for Tsunami Research are shown for comparison (Gica *et al.*, 2006). These are shown as two lines because the subfault distribution has two rows of subfaults along the trench axis. Events for which the rake angle is believed to have been assumed and not calculated are shown as empty circles. Also included in the comparison is the range of the geometric dip angle based on relocated hypocenters of thrust earthquakes and the trench axis as determined by Tichelaar and Ruff (1991). The historical earthquake depths are not shown because they cannot be compared to the reference depths. The hypocenter depth is by definition always greater than the reference depth.

In general, the computed source parameters show good agreement with those from the historical events and those used by PMEL. The strike angle varies between 307 and 19°. If the 90° rake angles from literature which are believed to have been assumed are disregarded from the historical data, the comparison with the computed rake angles is reasonable given the scatter of the points. As expected, the computed rake angle is the maximum deviation from a 90° of historical events. This is because slip partitioning is not included in the calculation of the rake angle. The computed rake angle indicates mostly reverse fault types, except near Southern Peru, where they indicate reverse left-lateral oblique fault types. The dip angles obtained from seismotectonic studies and used in this study vary between 13 and 20° and are all within the reported range for the geometric dip by Tichelaar and Ruff (1991). The dip angles of the historical events are generally higher than the values from seismotectonic studies. This is because the steepness of earthquake rupture areas increases with depth and the dip angles of the historical events are defined at the hypocenter located in the deeper region of the rupture areas. The dip is rather uniform which correlates well with the shallow subduction zones. The reference depth varies between 2 to 26 km and has an average value of approximately 9 km.

## 2.5 Subfault Distribution

For tsunami forecast, the subduction zone needs to be divided into subfaults with known source parameters. Considering the error in the source parameters and the limitations of the forecast technique, the subfault distribution does not have to match exactly every detail of past events, especially the smaller ones, but rather should capture the general pattern of the segmentation shown by the rupture areas and source parameters and be simple enough for operational purposes.

The tectonic setting of the Peru-Chile subduction zone is shown in Figure 4. The approximate rupture areas of the major thrust earthquakes are compiled from Abe (1972), Kelleher (1972), Dewey and Spence (1979), Delouis (1997), and Ruegg (1996, 2002). The rupture areas shown include those listed in Table 1 and other major events. The convergence rates and azimuths are obtained from DeMets *et al.* (1990, 1994) and the fracture zones are from Herron (1981). The fault areas tend to align with the trench axis and cover a region between approximately 20 and 150 km from the trench.

The subfault distribution in Figure 5 is based upon the rupture areas of large historic events, the presence of strike-slip faults, such as the Challenger Fracture Zone, and discontinuities in the geometry of the subducting oceanic plate. The approximate average length of the subfaults is 110 km, which is similar to Gica *et al.* (2006). Although Geist and Dmowska (1999) concluded that the heterogeneous slip distribution of shallow subduction earthquakes can have a significant impact on local tsunami waveforms, small scale features in the initial tsunami wave are filtered during the tsunami propagation, allowing the use of larger subfaults for far-field tsunami forecast. The present subfaults capture the approximate extent of earthquake ruptures but not entirely the heterogeneous slip distribution. The up-dip and down-dip limits are based on the thermal and structural models of Oleskevich (1999) and relocated depths of large thrust earthquakes (Tichelaar and Ruff, 1991).

## CHAPTER 3

### INVERSION METHOD

#### 3.1 Mareogram Database

The inverse method requires a database of mareograms, which are synthetic or pre-computed tsunami waveforms at specific locations due to unit slip of the subfaults. This study uses a linear long-wave model to generate the mareogram database. The governing equations in the spherical coordinates consist of a continuity equation and two momentum equations, given respectively by

$$\frac{\partial \zeta}{\partial t} + \frac{1}{R \cos \theta} \left[ \frac{\partial Q}{\partial \lambda} + \frac{\partial (P \cos \theta)}{\partial \theta} \right] = 0 \quad (1)$$

$$\frac{\partial Q}{\partial t} + \frac{gd}{R \cos \theta} \frac{\partial \zeta}{\partial \lambda} = 0 \quad (2)$$

$$\frac{\partial P}{\partial t} + \frac{gd}{R} \frac{\partial \zeta}{\partial \theta} = 0 \quad (3)$$

where  $t$  is time,  $\zeta$  is the sea surface elevation,  $d$  is the water depth,  $g$  is acceleration due to gravity,  $Q$  and  $P$  are fluxes in the longitudinal and latitudinal directions respectively,  $\theta$  is the latitude,  $\lambda$  is the longitude, and  $R$  is the earth radius. The depth-integrated equations are solved using a modified leap-frog finite difference scheme such as that discussed in Liu *et al.* (1995). The initial condition corresponds to a sea surface identical to the vertical seabed deformation. The land boundary is treated as a vertical wall in accordance with linear theory.

The computation used three levels of nested grids as shown in Figure 6. The first level is solved in spherical coordinates while the second and third are solved in Cartesian coordinates. The grid setup was carefully chosen to maximize the resolution wherever possible but also within practical computational and time constraints. This is very important because the resolution affects the tsunami wave especially in the near-shore regions. The first level covers the Pacific from the Peru-Chile source region to the

Hawaiian Islands at 2' resolution. The bathymetry is obtained from the 1' dataset GEBCO (2003). A finer 15" grid is used around the Hawaiian Islands and the bathymetry is obtained from the 5" dataset compiled by Japan Marine Science and Technology Center (JAMSTEC) and US Geological Survey (USGS). Because the Honolulu tide gauge recorded good signals of the tsunamis considered in this study, the island of Oahu is modeled at level 3 with 3" resolution. The JAMSTEC/USGS bathymetry is merged with the SHOALS/LIDAR dataset at 1 to 5 m resolution from the Joint Airborne Lidar Bathymetry Technical Center of Excellence. All datasets were converted to the WGS 84 datum and mean-sea level and merged using the Geographical Information System software ArcGIS 9.0. The data is subsequently gridded using the Generic Mapping Tools open source code described in Wessel and Smith (1991).

Figure 6 shows the tide gauge stations that recorded clear signals of the 1960 Valdivia-Chile tsunami, the 1995 Antofagasta-Chile tsunami, and the 2001 Atico-Peru tsunami. Only the stations in relatively open areas that can be resolved by the first-level bathymetry grid are considered. Synthetic mareograms were computed at the 17 stations for unit slip of the subfaults. To reduce the size of the mareogram, only the first 4 hours of data after the arrival time are saved at one minute intervals.

### 3.2 Adaptive Inverse Algorithm

The inverse algorithm is a non-negative regression of recorded tsunami waveforms against pre-computed mareograms to determine the slip distribution at the fault. Let  $m$  denote the number of subfaults and  $n$  the number of recorded tsunami waveforms at near-field stations. By assuming linearity in tsunami generation and propagation, the superposition of mareograms provides an approximation of the tsunami waveform at water-level station  $i$  as

$$a_i(t) = \sum_{j=1}^m A_{ij}(t + \Delta t_j) x_j \quad (4)$$

where  $t = 0$  is the initial time of the earthquake,  $\Delta t_j$  denotes the time when slip occurs at subfault  $j$ ,  $a_i(t)$  is the measured tsunami waveform at water-level station  $i$ ,  $x_j$  is the slip at subfault  $j$ , and  $A_{ij}(t)$  is the pre-computed mareogram at station  $i$  due to unit slip at subfault  $j$ . If the subfault dislocation occurs simultaneously at  $t = 0$ , Equation (4) reduces to the inverse approach

$$a_i(t) = \sum_{j=1}^m A_{ij}(t) x_j \quad (5)$$

originally proposed by Satake (1987).

The present inverse algorithm introduces additional degrees of freedom through  $\Delta t_j$  to better approximate the recorded waveforms. This allows for correction of errors in the initial estimation of the earthquake time and most importantly provides a more realistic description of the rupture process. For given  $\Delta t_j$ , the slip distribution  $x_j$  can be solved through a non-negative least-squares analysis as in the conventional approach. The optimum solution for  $\Delta t_j$  is found then by minimizing the root-mean-squared error

$$\text{RMSE} = \left\{ \frac{1}{n} \sum_{i=1}^n \frac{1}{L_i} \int_0^{L_i} \left( a_i(t) - \sum_{j=1}^m A_{ij}(t + \Delta t_j) x_j \right)^2 dt \right\}^{1/2} \quad (6)$$

where  $L_i$  is the duration of record  $a_i(t)$  starting at the tsunami arrival time. Wei *et al.* (2003) suggested that the record should cover at least the first wave of the tsunami. The solution space for  $\Delta t_j$  is subject to physical constraints related to the rupture process. The rupture must propagate contiguously from a subfault which may be constrained to within a certain radius from the earthquake epicenter. Benioff *et al.* (1961) estimated a rupture speed of 3 to 4 km/sec for the 1960 Chile tsunami and Song *et al.* (2005) estimated a speed of 1.25 to 3.5 km/sec for the 2004 Indian Ocean tsunami. In addition, the inverse algorithm can rule out subfaults that are outside of the rupture area based on comparison of arrival times in the mareograms and recorded waveforms. This is important because the conventional inverse method sometimes assigns artificial slip to subfaults outside the rupture area. Although the values are usually small, they are unrealistic and affect the slip

distribution in the rupture area and the resulting waveforms. Although the initial earthquake time determined from seismic data has accuracy much smaller than the temporal resolution of the recorded tsunami waveforms, the earthquake may actually consist of several sub-events each producing their own tsunami waves.

This is a Constrained Optimization Problem and the most straightforward solution approach is the Generate and Test algorithm (Tsang, 1995). This algorithm generates the entire solution space and eliminates combinations by applying the constraints. The advantage of this method is that it performs a complete search of the solution space and thus guarantees the optimal solution. Nevertheless, this approach is very inefficient because of the need to examine all possible combinations while only a few actually satisfy the problem constraints. A more efficient way to solve the problem is to use the constraints actively in defining the solution space. This approach minimizes unnecessary constraint testings and consequently reduces the size of the problem. First, the problem is reduced by eliminating subfaults which are outside of the earthquake rupture area by comparing the arrival times of the mareogram and the recorded tsunami waves. Because the rupture sequence is independent of the starting start, these can be separated in the algorithm to further reduce the problem. The user-specified rupture speed range is used to calculate all possible rupture sequences for a specific time. Then the start of the rupture is varied to create the entire solution space. Once this is done, the solution space is small enough that the optimal solution can be found in less than one second. Other optimization algorithms can be used for this problem such as the sequential quadratic programming method proposed by Powell (1978), but have difficulties with discrete and discontinuous solution spaces and may converge to a local solution. The presented approach is preferred because it guarantees the optimal solution but also has the advantages of being simple, providing information on the variance of the slip distribution in the solution space and being more than sufficiently fast for this application.

After the slip distribution is obtained from the adaptive inverse algorithm, an estimation of the amount of energy released in the earthquake can be obtained through seismic moment using the relation proposed by Kanamori (1977)

$$M_0 = \mu \sum_{j=1}^m \alpha_j x_j \quad (7)$$

where  $\alpha_j$  is the area of subfault  $j$ , and  $\mu$  is the shear modulus and is assumed to be 30 GPa for the Peru-Chile source region (e.g. Delouis *et al.* 1997). The moment magnitude is calculated from the seismic moment using the formula originally proposed by Hank and Kanamori (1979)

$$M_w = \frac{2}{3} \log_{10}(M_0) - 6.07. \quad (8)$$

The seismic moment and moment magnitude can be compared to the values reported from initial seismic data for validation of the inversion results.

Wei *et al.* (2001, 2003) extended the inverse algorithm of Satake (1987) to provide forecasts of tsunami waveforms at specific warning points away from the source. Once the slip distribution  $x_j$  and event time sequence  $\Delta t_j$  are obtained for Equation (4), the far-field waveforms can be estimated by superposition of the pre-computed mareograms as

$$b_k(t) = \sum_{j=1}^m B_{kj}(t + \Delta t_j) x_j \quad (9)$$

where  $b_k(t)$  is the predicted tsunami waveform at warning point  $k$  and  $B_{kj}(t)$  is pre-computed mareogram at warning point  $k$  due to unit slip of subfault  $j$ .

A Jackknife resampling technique is used to estimate the error in the inversion analysis (e.g., Efron, 1982; and Wu, 1986). For a “delete-1” jackknife technique, the  $l$ -th water-level record is removed from the  $n$  records in the original dataset to produce a slip distribution  $x_j^{-l}$

$$a_i(t) = \sum_{j=1}^m A_{ij}(t + \Delta t_j) x_j^{-l} \quad \text{for} \quad \begin{cases} i=1, 2, \dots, n, & l=1, 2, \dots, n \\ i \neq l, & j=1, 2, \dots, m \end{cases} \quad (10)$$

The  $l$ -th waveform at warning point  $k$  is given by

$$b_k^{-l}(t) = \sum_{j=1}^m B_{kj}(t + \Delta t_j) x_j^{-l}. \quad (11)$$

For the mean estimate, it can be shown that the jackknife bias is zero

$$b_k(t) \equiv \frac{1}{n} \sum_{l=1}^n b_k^{-l}(t). \quad (12)$$

The standard error  $s_k(t)$  at warning point  $k$  is then computed from

$$s_k(t) = \left\{ \frac{n-1}{n} \sum_{l=1}^n [b_k^{-l}(t) - b_k(t)]^2 \right\}^{1/2}. \quad (13)$$

The upper and lower bounds of the predicted waveform are thus given by

$$\zeta_k(t) = b_k(t) \pm t_{\alpha/2, \nu} \frac{s_k(t)}{\sqrt{n}} \quad (14)$$

where  $t_{\alpha/2, \nu}$  is the inverse of the Student's  $t$  cumulative distribution function corresponding to the  $(1 - \alpha)$  confidence and  $\nu = n - 1$  degrees of freedom. The same technique is applied to calculate the confidence-interval bounds at the near-field water-level stations. Tichelaar and Ruff (1989) showed that the jackknife technique provides the same standard deviation regardless of the number of waveforms dropped in the re-sampling scheme. A small standard deviation indicates consistent and reliable predictions.

In the event of an earthquake, the epicenter and the magnitude are determined through a network of seismometers within 15 minutes after the earthquake. The magnitude can be used to estimate the length of the rupture using the empirical relationships of Wells and Coppersmith (1994) for thrust earthquakes

$$\log_{10}(\text{Length}) = 0.58M_w - 2.42 \quad (15)$$

This in turn provides an estimate of the average slip using Equation (7). This information is sufficient to provide an initial wave forecast without any tide gauge data. Real-time water-level data containing the first tsunami wave will be available at several

tide gauges in the next two hours. The water-level records must be preprocessed to remove the tidal components and other oscillations to obtain the input tsunami signals. The preferred method in this study is a band-pass Butterworth filter with cut-off periods of 4 minutes and 4 hours. This method performs well with relatively long time series and with no gaps. Shorter time series or those with large gaps are first processed with a harmonic analysis and then a low-pass Butterworth filter with a cut-off periods of 4 minutes. Due to the short time series, only the two lunar diurnal and semidiurnal frequencies are used in the harmonic analysis. Despite the simplistic approach, this method performed much better than applying a band-pass digital filter or hindcasting the signal using a tidal model.

## CHAPTER 4

### RESULTS AND DISCUSSION

The inverse method has been proven to work well for the Japan-Kuril-Kamchatka and Alaska-Aleutian source regions despite the assumptions and simplifications (Wei *et al.*, 2001, 2003; Titov *et al.*, 2005; and Yamazaki *et al.*, 2006). High resolution tide gauge data of recent tsunami events are available along the South America coast. Of these, the 1995 Antofagasta-Chile and 2001 Atico-Peru events were recorded in Hawai'i. Prior to 1995, the 1960 Valdivia-Chile tsunami was well recorded by tide gauges as reported by Symons (1962). Therefore, this study uses the 1960, 1995 and 2001 events to test, compare, and validate the capability of the conventional and adaptive inverse methods. In the latter method, the rupture speed is constrained to a range of 2-6 km/sec for all three events. The location of the earthquake origin is left for the inverse algorithm to determine, except for the 1960 event for which the epicenter is specified.

#### 4.1 1960 Valdivia-Chile Tsunami

The Chile earthquake of May 22, 1960 is the largest in recorded history. This large underthrusting event ruptured a segment approximately 1000 km long in Southern Chile (Plafker, 1972). The resulting tsunami produced runup heights of 10 to 20 m at several locations between Isla Guafo and Isla Mocha near the source (Plafker, 1970). The tsunami traveled across the Pacific and produced a maximum runup height of 10.7 m in Hilo, Hawai'i (Walker, 2004).

Due to the lack of tide gauge records near the earthquake, the stations at Callao and La Libertad are used in the inverse analysis despite their distance from the source. Two stations is the minimum number required for the inversion and three is the minimum required to calculate confidence intervals using the jackknife re-sampling technique (Wei *et al.*, 2003). For this reason, the confidence intervals could not be calculated for the 1960 event. The fact that the two tide gauges are on the same side of the rupture area may give

rise to a poor constrained inverse problem, because adjustments in the timing and location of the rupture may have similar effects to the solution. As a result, the initial rupture was constrained to within 20 km of the epicenter. The great 1960 Chile earthquake followed a 33-hour sequence of earthquakes that began with a  $M_w$  8.1 foreshock on May 21 10:02:52 (Cifuentes and Silver, 1989). The initial earthquake time used in both inverse methods is May 22 at 19:10:40 and is taken from Cifuentes (1989).

The adaptive inverse algorithm identified the rupture area over subfaults 1 to 6. The convergence of the slip distribution in Figure 7 indicates that the RMSE is not a random function but rather a semi-continuous multidimensional surface with a unique optimal solution. The results are not very sensitive to the correction on the rupture time. Table 2 shows a comparison of the inversion results from the two methods. The slip distribution from the conventional method does not produce any slip at subfault 6 which is where the epicenter is located. The adaptive inverse does calculate a slip for this subfault. This is probably because the actual limit of the rupture is within subfault 6. The rupture in the optimal solution includes subfaults 1 to 6 and shows a time lag of 2 to 4 minutes with respect to the reported earthquake time. The adaptive inverse algorithm can only produce a minor improvement over the conventional approach because the rupture duration and time lag with respect to the initial earthquake time are small in comparison with the long wave period of more than 2 hours. The computed earthquake magnitude of  $M_w$  9.15 is smaller than the  $M_w$  9.35 reported by Barrietos and Ward (1990). Because the details of the earthquake rupture and asperity distribution are not known, the computed slip distribution and timing cannot be verified.

Figure 8 shows an illustration of the adaptive inverse algorithm. Figures 8a and 8b show the unit-slip mareograms plotted with respect to the arrival times. It can be seen that the waves from the different subfaults are very similar at each tide gauge, while the two locations exhibit different characteristics of the waveforms. This indicates the strong influence of the location on the wave conditions that need to be captured in the

mareograms. When the mareograms are plotted with respect to the input earthquake time in Figures 8c and 8d, the effects of the timing become obvious and this illustrates advantage of the adaptive scheme to reconstruct the recorded tsunami signals.

Figure 9 compares the inversion results from the conventional inverse method and the adaptive inverse method. The waveforms from both methods are very similar and provide very good match with the recorded data. The greatest differences occur at Callao after 400 minutes from the start of the earthquake. Even though the RMSE is improved only slightly, the differences in the slip distributions are up to 30%. Table 2 also shows the correlation coefficient  $R$  between the computed and recorded waveforms (see Appendix B). The correlation coefficient is also improved by the adaptive inverse method although only slightly. It should be noted that the inverse method is capable of fitting the waveform at La Libertad for more than 400 minutes. The far-field predictions for the 1960 Chile tsunami event are shown in Figure 10 using the slip distribution and timing obtained from the conventional and the adaptive inverse algorithms. The computed tsunami waveforms have been shifted to match the recorded arrival time. The reason for the errors in the tsunami arrival times is unknown but they are very small compared to the propagation times. Errors in the computed arrival time were also reported by Yamazaki *et al.* (2006). Both inverse methods produce similar waveforms and very good agreement with the recorded wave amplitude but produce a small phase shift as a result of the 2 to 4-min lag between the earthquake and tsunami generation.

#### 4.2 1995 Antofagasta-Chile Tsunami

The earthquake of July 30, 1995 near the city of Antofagasta, Chile had a moment magnitude of 8.0 to 8.1 (e.g., Carlo *et al.*, 1999). The event produced tsunami waves of 2 to 2.5 m high along the coast from Mejillones to Taltal (Delouis *et al.*, 1997). The near-field tide gauge stations at Arica, Iquique, Callao, Caldera and Valparaiso recorded good signals of the tsunami for use in the inverse analysis. Other near-field stations such as

Lobos de Afuera and Talcahuano are not considered because of significant local oscillations and questionable data quality. Also the Antofagasta station was inside the earthquake rupture area, where the tsunami waveforms cannot be reproduced accurately by the numerical model, and are therefore excluded from the analysis. The initial earthquake time 5:11:57 is obtained from the Harvard Centroid Moment Catalog.

The algorithm selected subfaults 18 and 19 to represent the rupture area. Your figure shows 17 and 18. Figure 11 shows the convergence of the adaptive inverse method. The improvement from the adaptive inverse method over the conventional approach is very significant. The results show a clear pattern of the slip timing adjustment as the algorithm converges to the best solution. There is an apparent 4 min lag between the initial earthquake time and the formation of the tsunami wave. Because of the small size of the fault area, the effect of rupture propagation is not very pronounced. However, the adaptive inverse algorithm is able to locate the earthquake origin and the timing of the slip inside the rupture zone correctly. Carlo *et al.* (1999) and Delouis *et al.* (1997) showed that the rupture of the 1995 tsunami started in the northern part of the rupture area and propagated south over a 1-min duration as shown in the results of the adaptive inverse method.

Figure 12 shows the near-field inversion results using the conventional and adaptive inverse algorithms. The computed water levels from the adaptive inverse algorithm give good agreement with the recorded data, considering the assumption of linearity and the resolution of the model grid at 2'. The performance of the conventional inverse algorithm is reasonable, but has much larger confidence intervals and is not nearly as good as those produced by the adaptive inverse algorithm. This is because the 4 min lag time in tsunami generation is comparable to the period of the tsunami waves. Table 2 shows a comparison of the results of the conventional and adaptive inverse algorithms. The slip distributions are quite different. The significant improvement of the inversion results by including the timing of rupture is evident in the RMSE and correlation coefficients. The adaptive

inverse method gives a moment magnitude of 8.03, which is larger than 7.93 and is inside the reported range of 8.0 to 8.1.

Figure 13 shows the far-field tsunami waveforms based on the results from the conventional and adaptive inverse methods. The comparison between the historical records and the two sets of hindcast waveforms is good in general and indicates the validity of the inverse method as a tsunami forecast tool. The results obtained from the adaptive inverse algorithm show much smaller confidence interval bounds and better agreement with the recorded data. The large differences between the predicted and recorded waveforms at the tide gauge stations of Easter Island and Lobos de Afuera are likely due to insufficient grid resolution. The results at stations with higher grid resolutions produced good comparisons between the predicted and recorded tsunami waveforms.

### 4.3 2001 Atico-Peru Tsunami

The June 23, 2001 earthquake of Peru occurred near the coastal town of Atico and had a moment magnitude of 8.2 (Kikuchi and Yamanaka, 2001). This earthquake took place at a zone of the plate boundary where no major rupture had occurred since the 1868 earthquake of magnitude between 8.2–8.4 (Dorbath *et al.*, 1990, Comte and Pardo, 1991). The earthquake produced a destructive local tsunami, but only minor wave amplitudes in Hawai'i. The stations at Antofagasta, Caldera, Callao, Iquique, Coquimbo, Corral, and Valparaiso provide near-field tsunami signals for the inverse analysis. The Arica station was not included in the analysis because it is too close to the rupture area. The initial earthquake time of 20:34:23 is obtained from the Harvard Centroid Moment Catalog.

Figure 14 shows the convergence of the near-field inversion results using the adaptive inverse method. The rupture apparently occurs at subfaults 28 and 29. The effects of subfault 30 diminish as the solution converges. The adaptive inverse algorithm significantly reduces the RMSE and correlation coefficient. A comparison of the near-

field inversion results using the conventional and adaptive inverse algorithms is shown in Figure 15. The adaptive inverse algorithm produces better agreement with the records especially at stations Callao and Corral. The greatest differences between the hindcast and recorded waveforms occur at the crest of the waves. This may be explained partially by the use of a linear model.

A comparison of the slip distribution and RMSE using both inverse methods is shown in Table 2. The slip distributions are very different. In addition, there is a 3-min time lag between the start of the earthquake and the formation of the initial tsunami wave. This apparent time lag is observed in all three events. The cause of this time lag is unclear but may have to do with the seabed deformation process or tsunami wave generation. The adaptive inverse method is able to calculate the origin of the earthquake at subfault 29. The results are consistent with the report by Giovanni *et al.* (2002) that the earthquake started in the northern part of the rupture and propagated southeast. The calculated far-field tsunami waveforms using both the standard and the adaptive inverse methods are shown in Figure 16. The results from the AIM are in general better, although the waveforms from the conventional inverse method are also surprisingly good despite the difference in the slip distributions. The adaptive inverse method produces smaller confidence intervals than the conventional method.

## CHAPTER 6

### CONCLUSIONS AND RECOMMENDATIONS

The historical events and seismotectonics have shown that the interplate thrust mechanism is dominant for trans-Pacific tsunamigenic earthquakes in the Peru-Chile source region. The subduction zone runs along the South American trench from 9 to 46°S. The shallow seismically coupled region may be approximated by rectangular subfaults with strike angles parallel to the trench, motions in the direction of plate convergence, and low-dip angles for the implementation of the inverse algorithm.

The performance of the conventional and adaptive inverse algorithms is examined through hindcast analyses of the 1960 Valdivia-Chile, 1995 Antofagasta-Chile, and 2001 Atico-Peru tsunamis. Both inverse methods produce good results and demonstrate the capability of the inverse methods for tsunami forecast using tide-gauge data. The adaptive inverse algorithm, which provides additional degrees of freedom to resolve the time sequence of tsunamigenic earthquake, performs much better for the 1995 and 2001 tsunamis events and equally well for the 1960 event compared to the conventional method. The largest differences in the results are for the near-field stations, where the computed waveforms may differ in shape, phase and amplitudes. In the far-field, the two methods produce very similar waveforms but with different amplitudes and phases.

The adaptive inverse algorithm produces a better fit at the near-field water-level stations and consequently a better estimate of the earthquake magnitude. Although the effect of rupture propagation is not very significant for the tsunami events studied, the adaptive inverse algorithm produces significantly better results for the 1995 and 2001 events, because it allows for a lag between the initial earthquake and the formation of the initial tsunami wave. This time lag is more important for smaller tsunamis, which have shorter wave periods such as the 1995 and 2001 events, but does not have a significant effect on larger tsunamis with longer periods as in the 1960 tsunami. This allows the

adaptive inverse algorithm to perform well for large as well as moderate tsunamigenic events.

It is important to state that the subfaults have been designed for far-field tsunami forecast and not for near-field or local tsunamis, which would require a smaller subfault size to capture the asperity distribution (Geist, 2005). This is one of the reasons why it is not possible to match tide gauges that are too close to the tsunami source. If the adaptive inverse method is to be used for near-field tsunami warning, normal fault earthquakes should also be incorporated into the mareogram. This means adding additional subfaults with their corresponding source parameters. The inverse algorithm would then select the correct fault mechanism, but would require an additional constraint to enforce a single source mechanism throughout the rupture zone.

Table 1. Source parameters for major tsunamigenic earthquakes ( $M \geq 7.5$ ) in the Peru-Chile subduction zone in the last 100 years.

Zone	Earthquake	Date	Type	Lat. (°S)	Long. (°W)	Mag.	Depth (km)	Strike (°)	Dip (°)	Rake (°)	Length (km)	Width (km)	Reference		
Central Peru (9-15°S)	1970	May-31	Normal			Ms 7.8	33	340	53	90	130	60-80	Abe (1972)		
				9.18	78.82	Mw 7.9	43	340	37	90			Seno and Yoshida (2004)		
				9.36	78.87									Dewey and Spence (1979)	
							<50							Beck and Ruff (1989)	
	1996 Chimbote	Feb-21	Thrust									165	80	Dewey and Spence (1979)	
				9.95	80.23	Mw 7.5	15.0	335	14	88			HCMT		
	1966	Oct-17	Thrust			Ms 7.5	33	335	12	90	80	80	40	Delouis <i>et al.</i> (1997)	
						Ms 8.0	10-30								Abe (1972)
															Beck and Ruff (1989)
				10.92	78.79										Dewey and Spence (1979)
	1940	May-24	Thrust	11.22	77.79	Ms 8.0	10-30	340	20	90				Beck and Ruff (1989)	
												280	140		Chlieh <i>et al.</i> (2004)
	1974	Oct-3	Thrust			Ms 7.8		340	17	90					Beck and Ruff (1989)
				12.39	77.66							270	65		Dewey and Spence (1979)
						10-25								Beck and Ruff (1989)	
1942	Aug-24	Thrust	15.5	75	8.0-8.2	30-35	345	25	95	<150				Swenson and Beck (1996)	
			15	76	8.3		325	20	87					Okal (1992)	
Southern Peru (15-18°S)	1996	Nov-12	Thrust	15.04	75.37	Mw 7.7	37.4	312	33	55				HCMT	
												135	90		Chlieh <i>et al.</i> (2004)
	1913	Jun-8	Thrust	17.0	74.0	7.9									Kellerher (1972)
												130	110		Chlieh <i>et al.</i> (2004)
	2001 Atico	Jun-23	Thrust	16.15	73.4	Mw 8.35	15-37	319	13	76	240	110			Ruegg <i>et al.</i> (2002)
						Mw 8.2						320	100		
16.15				73.40	Mw 8.2	30	309	21	61	200	100			Kikuchi & Yamanaka (2001)	
			17.28	72.71	Mw 8.4	29.6	318	14	79				HCMT		

Table 1. (Continued).

Zone	Earthquake	Date	Type	Lat. (°S)	Long. (°W)	Mag.	Depth (km)	Strike (°)	Dip (°)	Rake (°)	Length (km)	Width (km)	Reference			
Northern Chile (18-23°S)	<b>Seismic Gap</b>															
Central Chile (23-35°S)	1995 Antofagasta	Jul-30	Thrust	24.17	70.74	Mw 8.0	28.7	354	22	87			HCMT			
						Mw 8.1	26.0		22			180-200		Carlo <i>et al.</i> (1999)		
				23.43	70.48	Mw 8.1	36.0	8	19	110	180	70		Ruegg <i>et al.</i> (1996)		
						Mw 8.0	10-50	3	17	97	165	95		Delouis <i>et al.</i> (1997)		
	1987	Mar-05	Thrust	24.38	70.93	Mw 7.5	41.9	12	23	106			HCMT			
	1918	Dec-4	Thrust	26.0	71.0	Ms 7.6						125	75	Abe (1972) Chlieh <i>et al.</i> (2004)		
	1983	Oct-4	Thrust	26.01	70.56	Mw 7.6	38.7	9	20	110				HCMT		
	1922 Atacama	Nov-11	Thrust	28.5	70	Ms 8.3	0-40	0	20	90				Beck <i>et al.</i> (1998)		
				28.31	70.28	Mw 8.7	57								Lockridge (1985) Chlieh <i>et al.</i> (2004)	
	1943 Illapel	Apr-6	Thrust	30.75	72.0	Ms 7.9	<40	340-360	15-25	80-100	360	260	100	Beck <i>et al.</i> (1998) Chlieh <i>et al.</i> (2004)		
															Abe and Noguchi (1983)	
	1906 Valparaiso	Aug-17	Thrust	33.0	72.0	Ms 8.4						260	100	Chlieh <i>et al.</i> (2004)		
													200	70	Chlieh <i>et al.</i> (2004)	
	1985	Mar-03	Thrust	33.92	71.71	Mw 7.9	40.7	11	26	110				HCMT		
	1928 Talca	Dec-1	Thrust			Mw 7.9	<30	0-20	20-30	90	<150				Beck <i>et al.</i> (1998)	
				35.0	72.0	Ms 8.0									Abe (1981) Chlieh <i>et al.</i> (2004)	
					Ms 7.9						170	85	Chlieh <i>et al.</i> (2004)			
Southern Chile (>35°S)	1960 Valdivia	May-22	Thrust			Mw 9.55	<50	10	10	70-90	800	200		Kanamori and Cipar (1974)		
						Mw 9.35		7	20	105	850	130			Barrietos and Ward (1990)	
				38.31	72.65	Mw 9.7	44								Lockridge (1985)	
				38	72.2	Mw 9.6	23	7	12	90	920	120			Cifuentes (1989)	
				39.0	74.5								1055	240		Duda (1963)
						Ms 8.5	60	10	20	110	1000	120				Plafker (1972)

Table 2. Comparison of slip distributions obtained from the conventional and adaptive inverse methods. The numbers in parenthesis corresponds to the time lags of subfault motions from the initial earthquake time.

Event	1960 Valdivia-Chile		1995 Antofagasta-Chile		2001 Atico-Peru	
Inverse Method	Conventional	Adaptive	Conventional	Adaptive	Conventional	Adaptive
<b>Slip Distribution</b>	$x_3(0) = 15.48$	$x_6(2) = 2.19$ $x_5(3) = 15.79$	$x_{19}(0) = 3.48$	$x_{19}(4) = 2.51$	$x_{30}(0) = 0.81$	$x_{29}(3) = 2.65$ $x_{28}(4) = 5.67$
	$x_4(0) = 13.95$	$x_4(3) = 13.97$	$x_{18}(0) = 0.37$	$x_{18}(5) = 2.85$	$x_{29}(0) = 4.84$	
	$x_3(0) = 8.81$	$x_3(4) = 11.28$	$x_{17}(0) = 0.07$		$x_{28}(0) = 1.04$	
	$x_2(0) = 24.71$	$x_2(4) = 26.36$				
	$x_1(0) = 29.65$	$x_1(4) = 26.15$				
<b>R</b>	0.823	0.832	0.666	0.904	0.515	0.657
<b>RMSE</b>	0.1896	0.1854	0.1231	0.0707	0.1365	0.1202
<b><math>M_w</math> - Inversion</b>	9.14	9.15	7.93	8.03	8.11	8.17
<b><math>M_w</math> - Literature</b>	9.35 – 9.7		8.0 - 8.1		8.2 – 8.4	

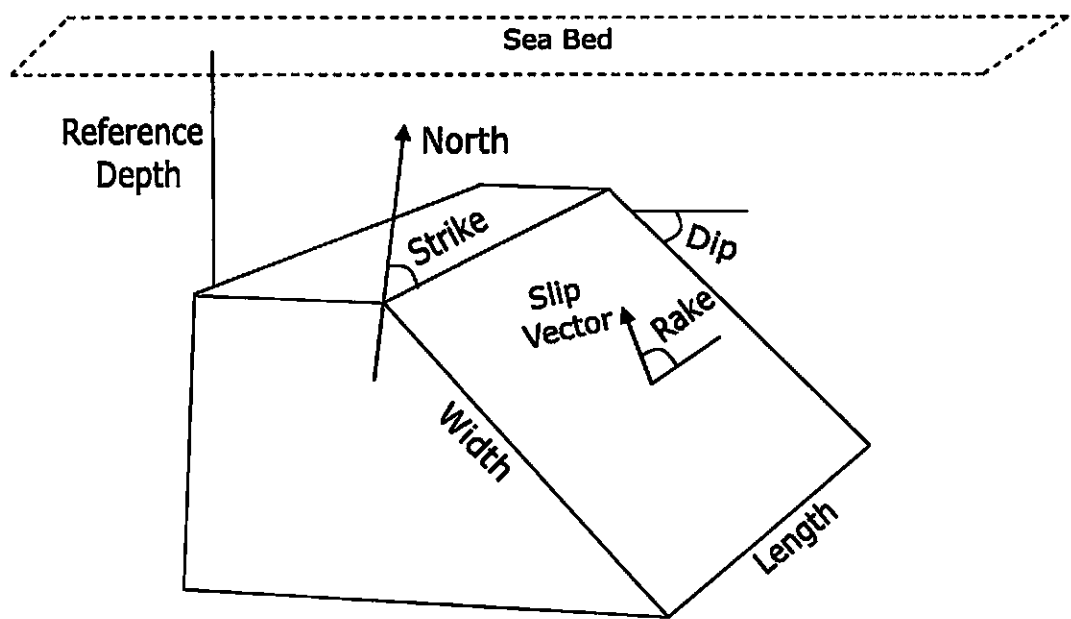


Figure 1. Definition sketch of a finite rectangular fault model.

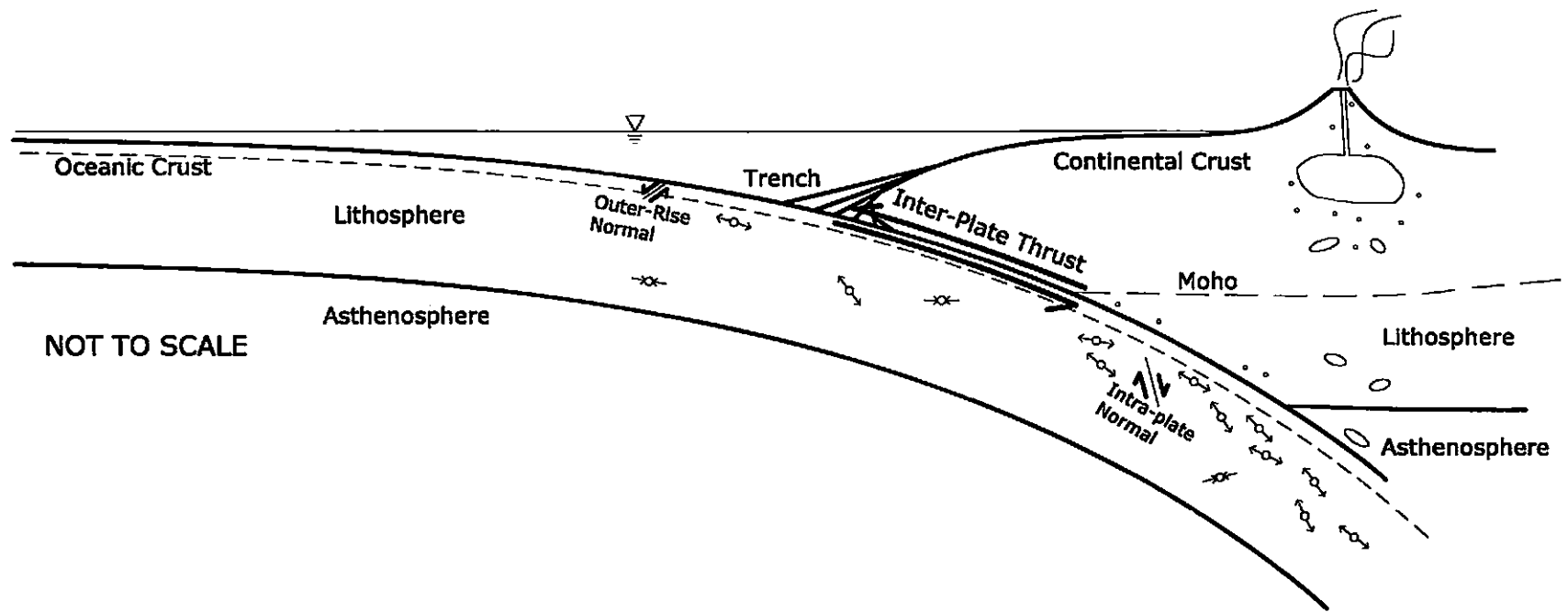


Figure 2. Schematic of a typical cross-section of the Peru-Chile subduction zone.

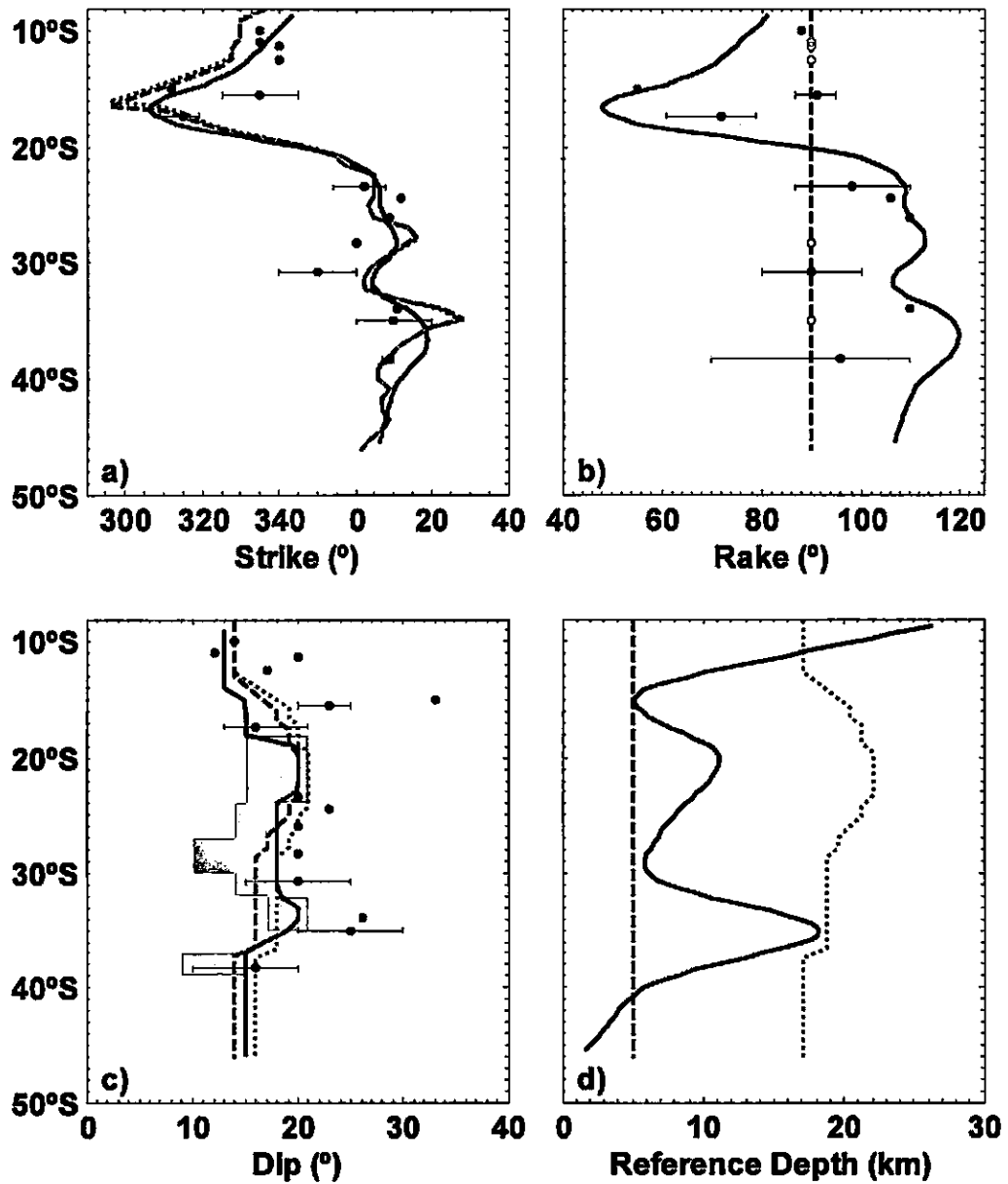


Figure 3. Comparison of source parameters of the Peru-Chile subduction zone. (a) Strike angle. (b) Rake angle. (c) Dip angle. (d) Reference depth. —, computed values; ●, historical events from Table 1; ○, historical events from Table 1 with assumed rake angles; - - - - -, up-dip, ······, down-dip source parameters from Gica *et al.* (2006); - · - · - ·, 90° rake; ■, Tichlaar and Ruff (1991).

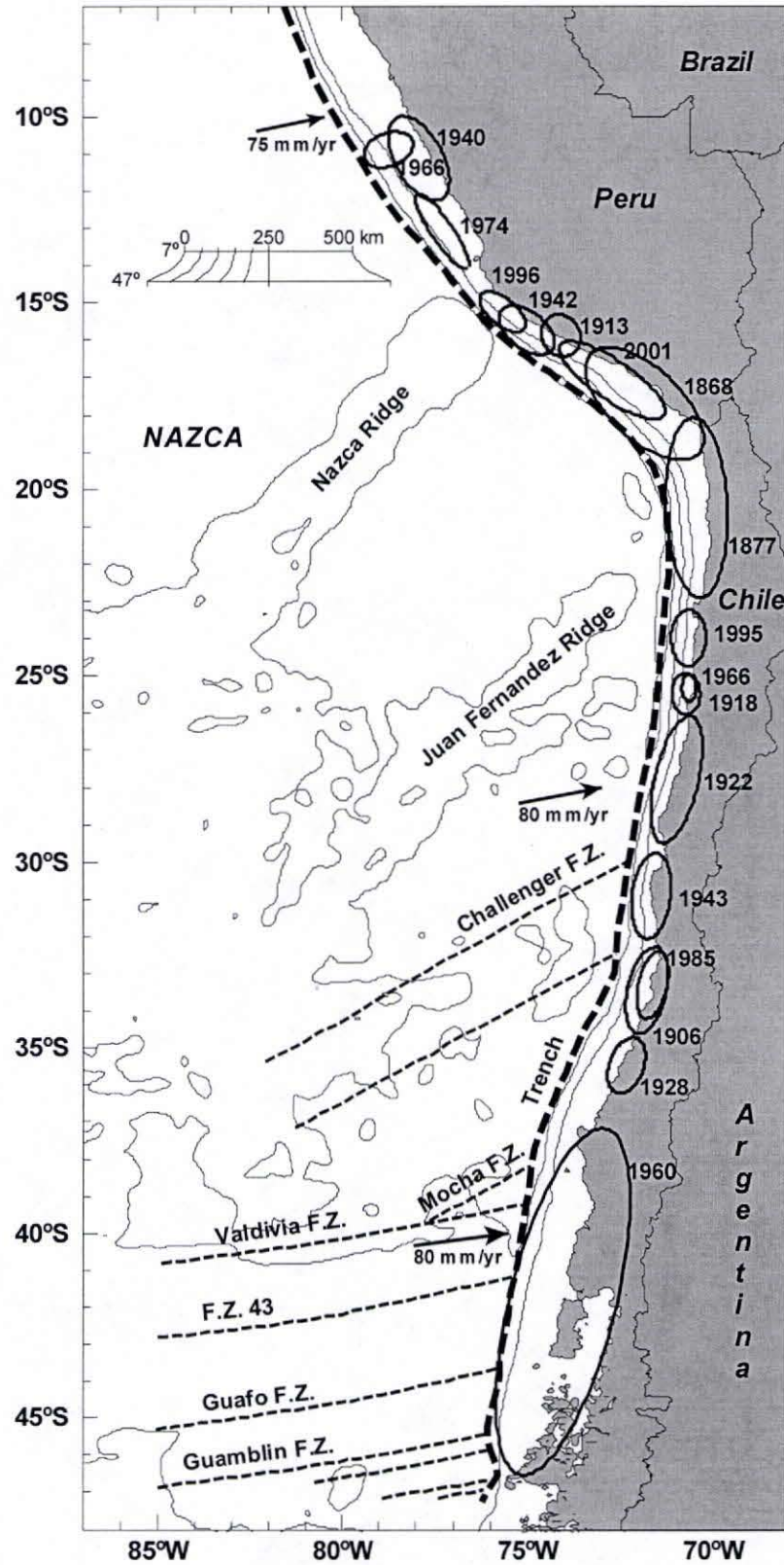


Figure 4. Tectonic setting and approximate fault areas of major earthquakes in the Chile-Peru subduction zone.

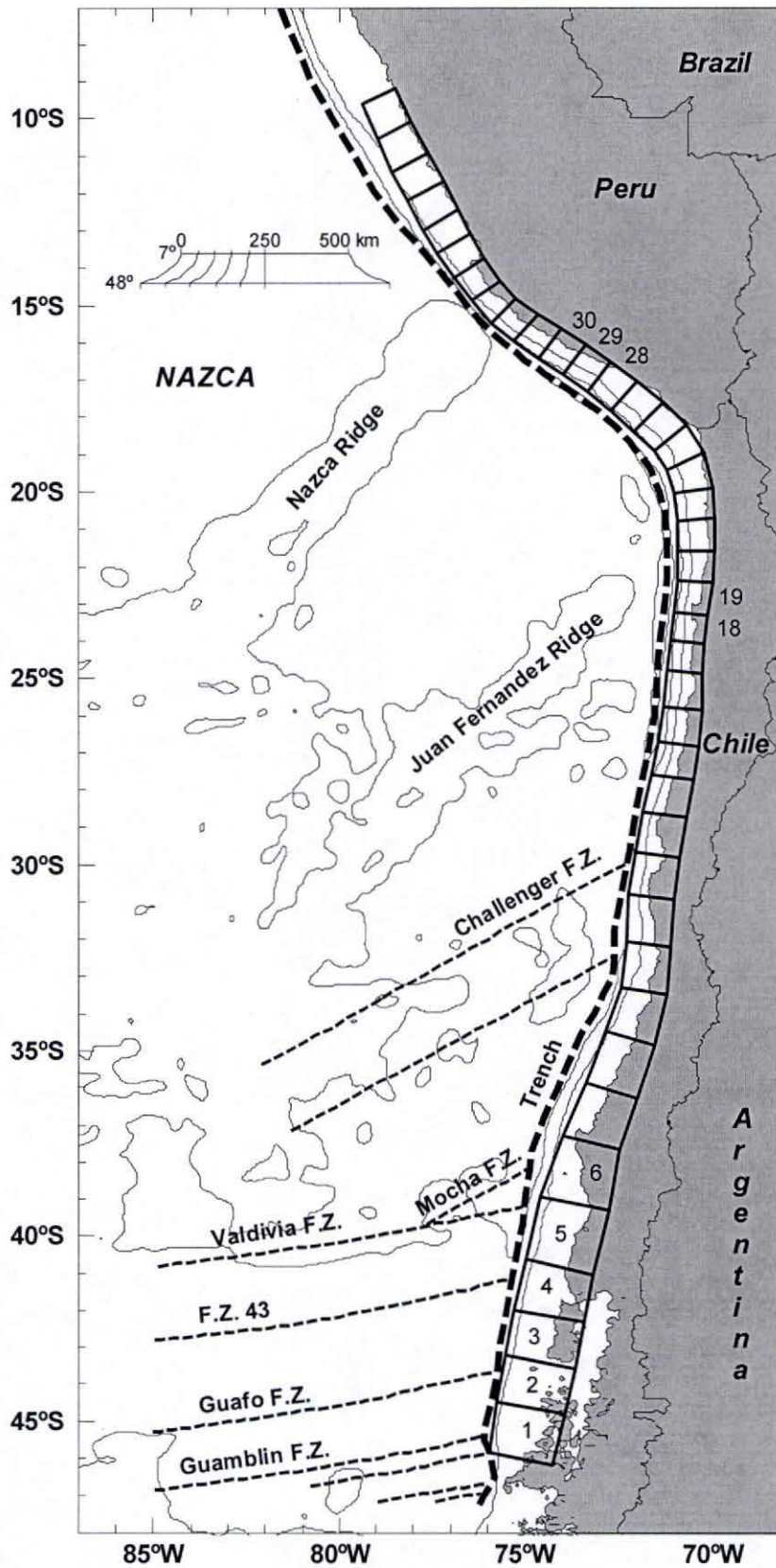


Figure 5. Subfault distribution for the Peru-Chile subduction zone.

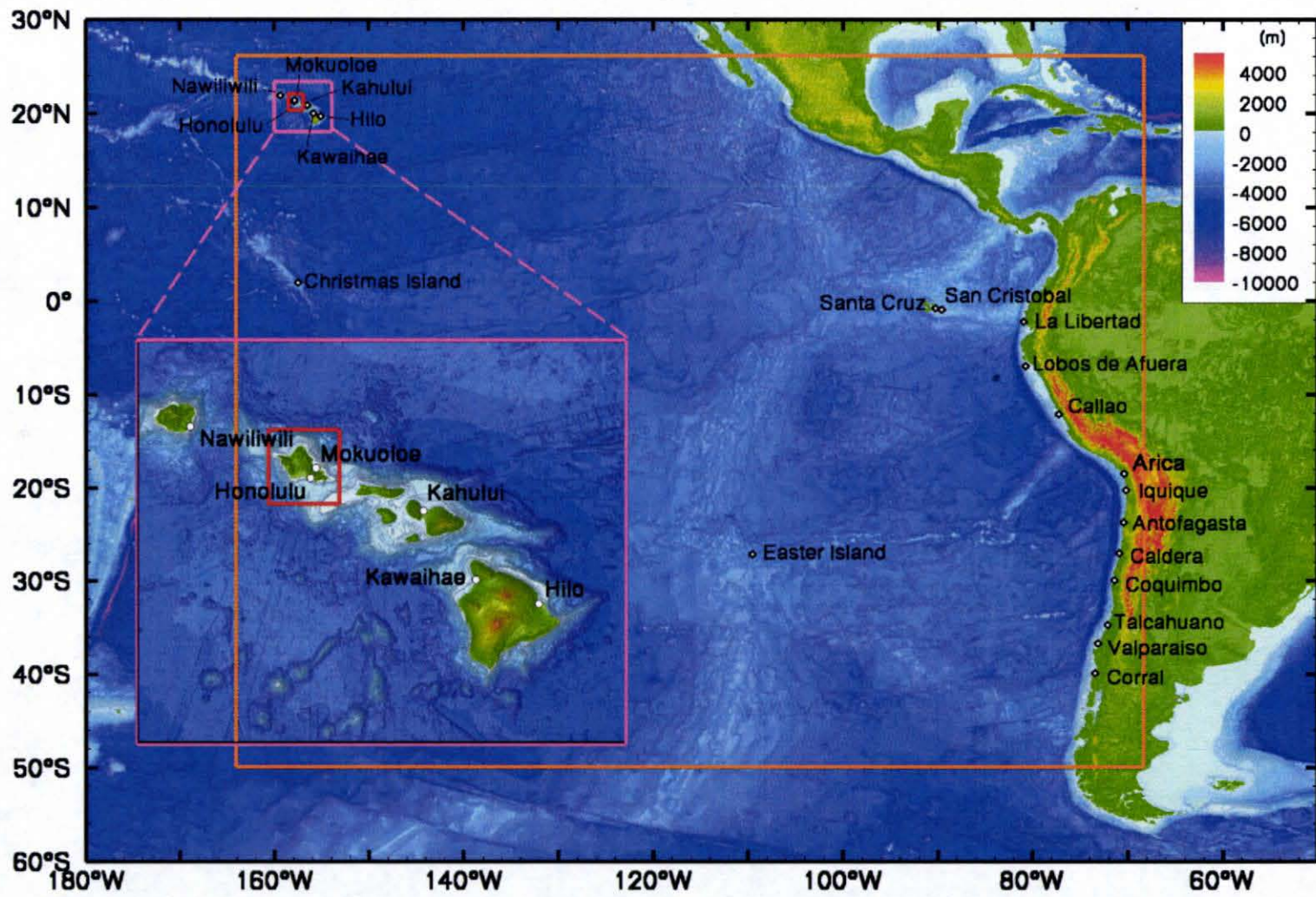


Figure 6. Computational grid system and water-level stations used in the inverse analysis. —, first layer; —, second layer; —, third layer; ○, tide gauge stations.

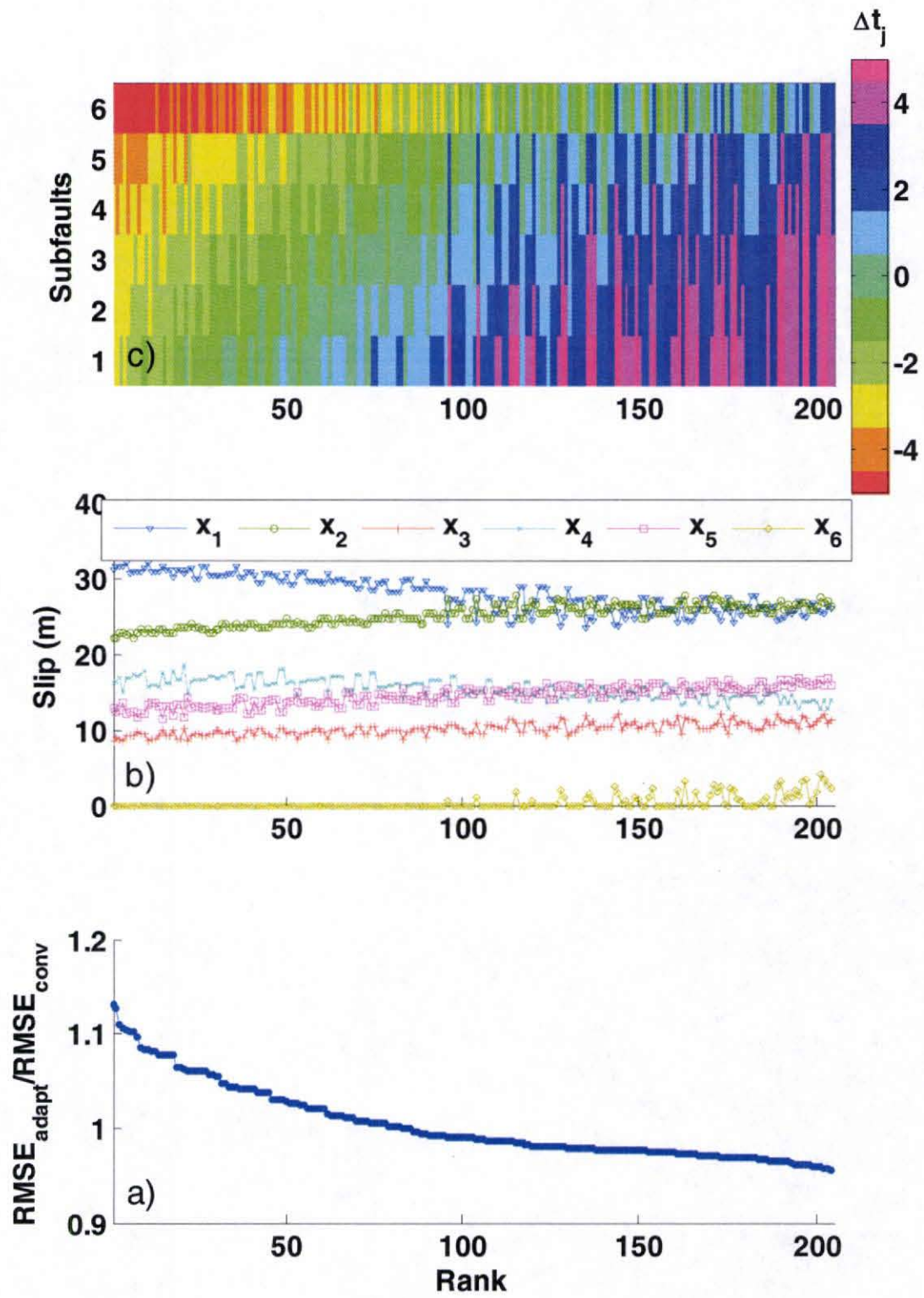


Figure 7. Convergence of the adaptive inverse method for the 1960 Valdivia-Chile tsunami.

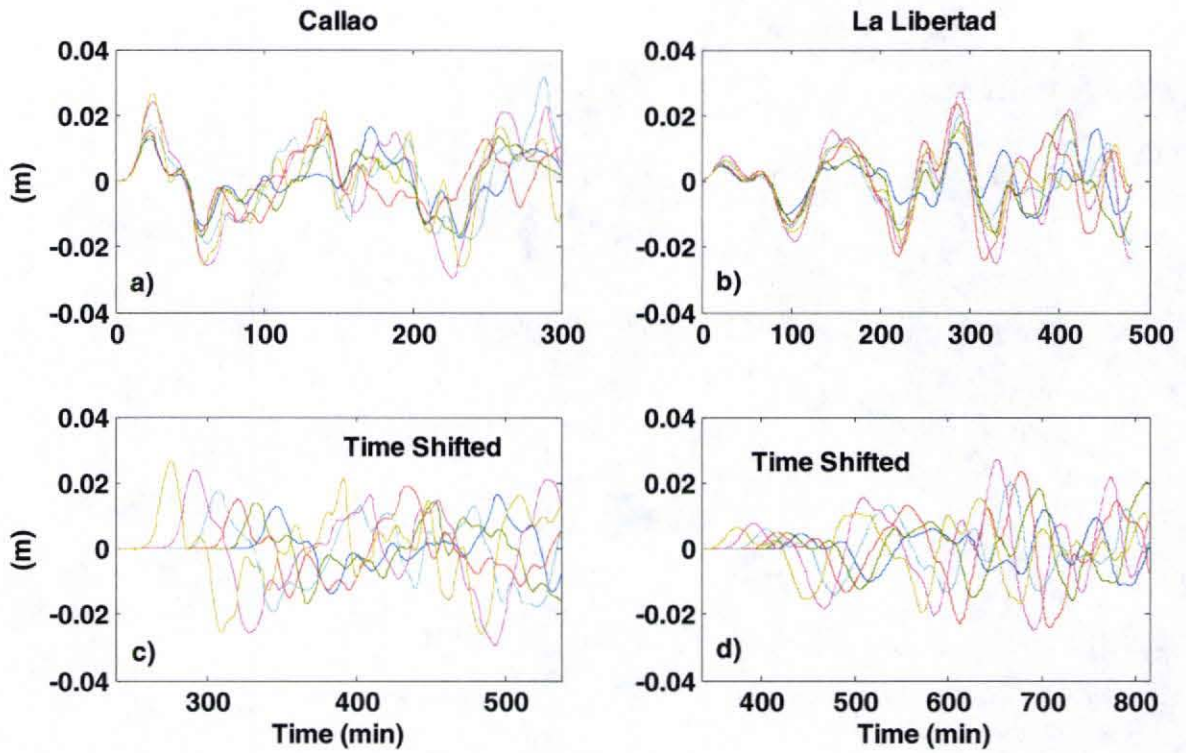


Figure 8. Mareograms and computed waveforms at near-field tide gauges for the 1960 Valdivia-Chile tsunami. —, subfault 1; —, subfault 2; —, subfault 3; —, subfault 4; —, subfault 5; —, subfault 6.

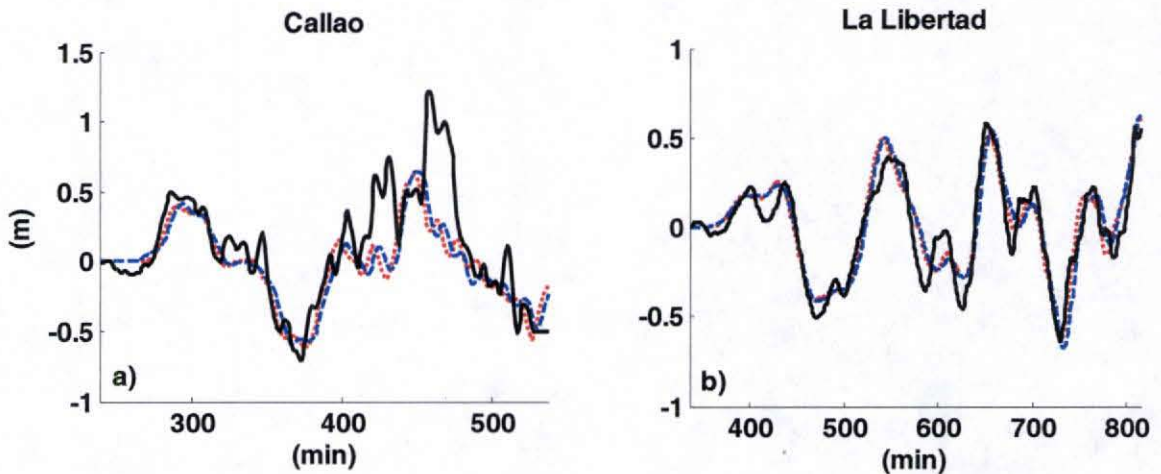


Figure 9. Computed and recorded waveforms at near-field tide gauges for the 1960 Valdivia-Chile tsunami. —, recorded tsunami wave; ..... , Conventional Inverse Method; - - - - , Adaptive Inverse Method.

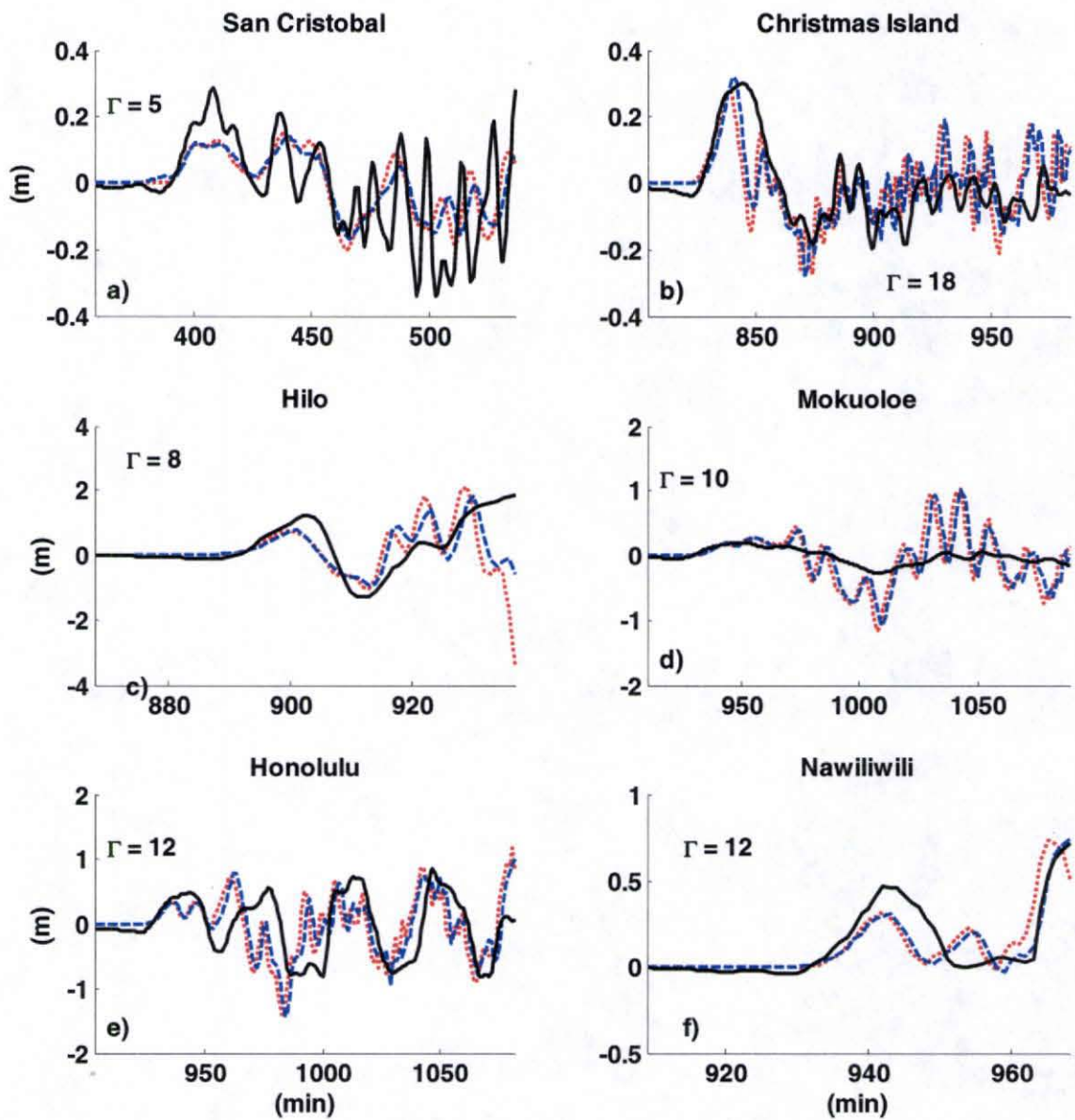


Figure 10. Computed and recorded waveforms at far-field tide gauges for the 1960 Valdivia-Chile tsunami.  $\Gamma$  indicates time shifts of computed waveforms to adjust for arrival times. —, recorded tsunami wave; ..... , Conventional Inverse Method; - - - - , Adaptive Inverse Method.

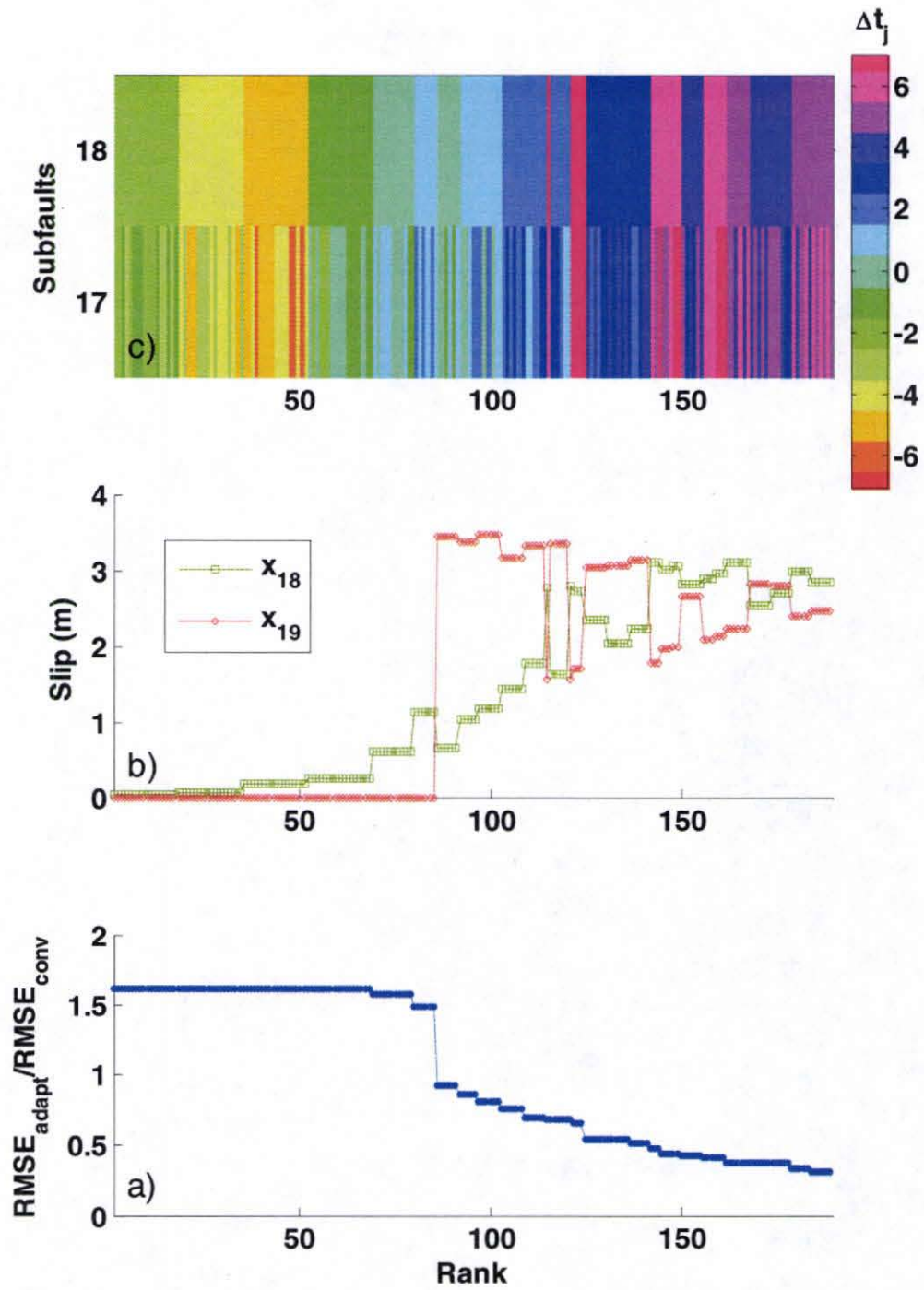


Figure 11. Convergence of the adaptive inverse method for the 1995 Antofagasta-Chile tsunami.

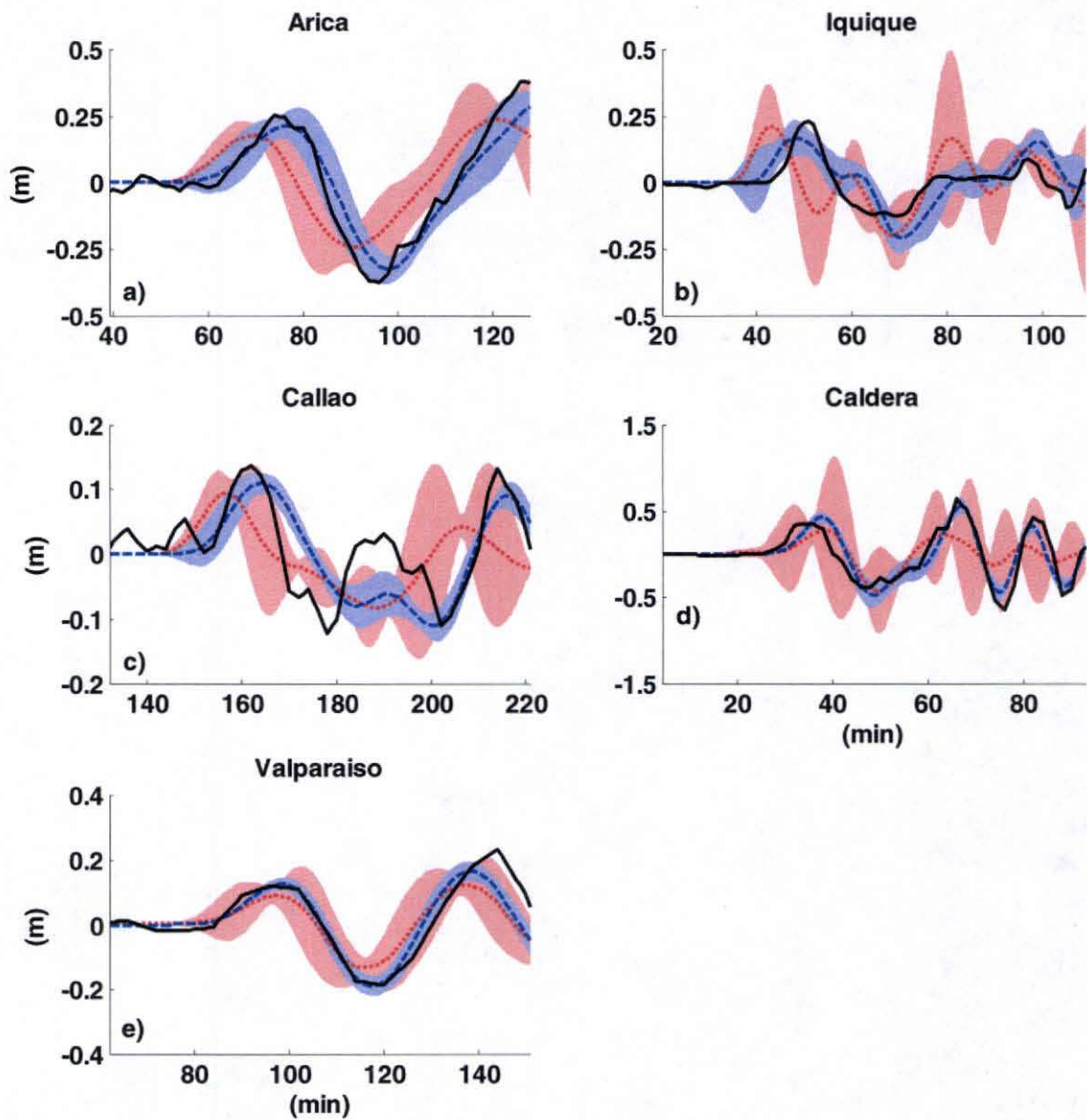


Figure 12. Computed and recorded waveforms at near-field tide gauges for the 1995 Antofagasta-Chile tsunami. ..... CIM; ----, AIM; ■■■■, 95% confidence interval for CIM; ■■■■, 95% confidence interval for AIM.

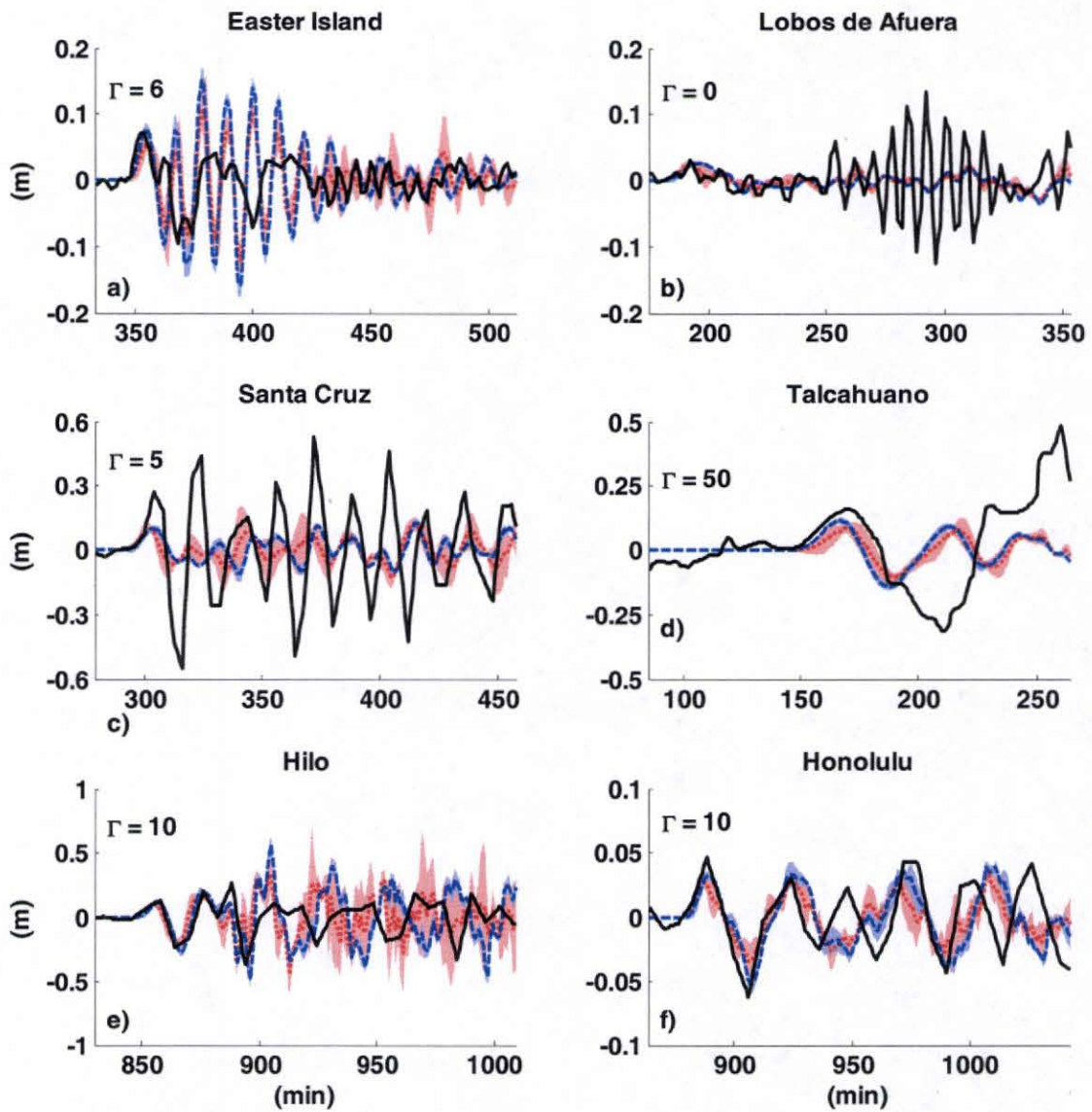


Figure 13. Computed and recorded waveforms at far-field tide gauges for the 1995 Antofagasta-Chile tsunami.  $\Gamma$  indicates time shifts of computed waveforms to adjust for arrival times. ....., CIM; - - - -, AIM; , 95% confidence interval for CIM; , 95% confidence interval for AIM.

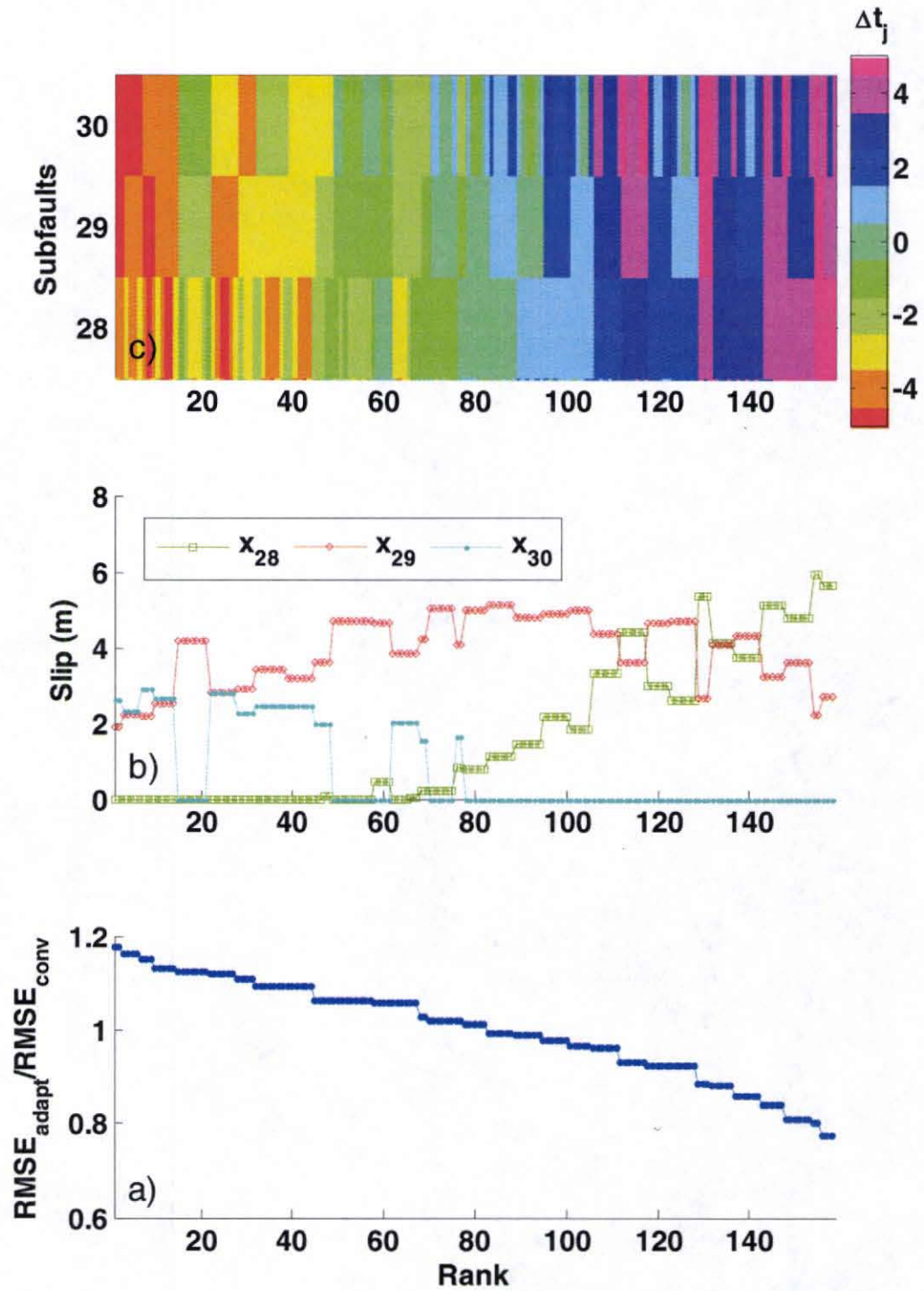


Figure 14. Convergence of the adaptive inverse method for the 2001 Atico-Peru tsunami.

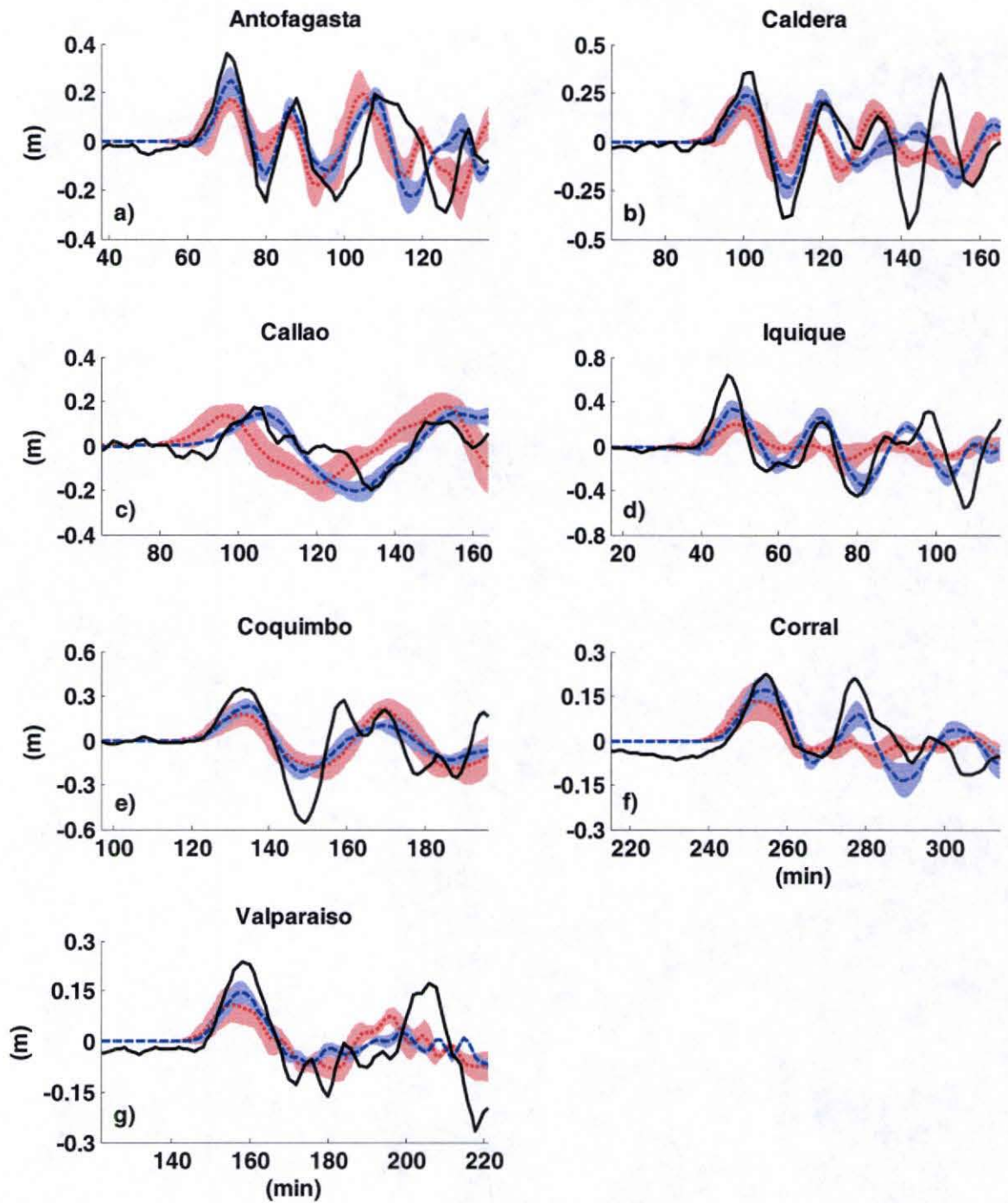


Figure 15. Computed and recorded waveforms at near-field tide gauges for the 2001 Atico-Peru tsunami. ...., CIM; ----, AIM; ■■■, 95% confidence interval for CIM; ■■■, 95% confidence interval for AIM.

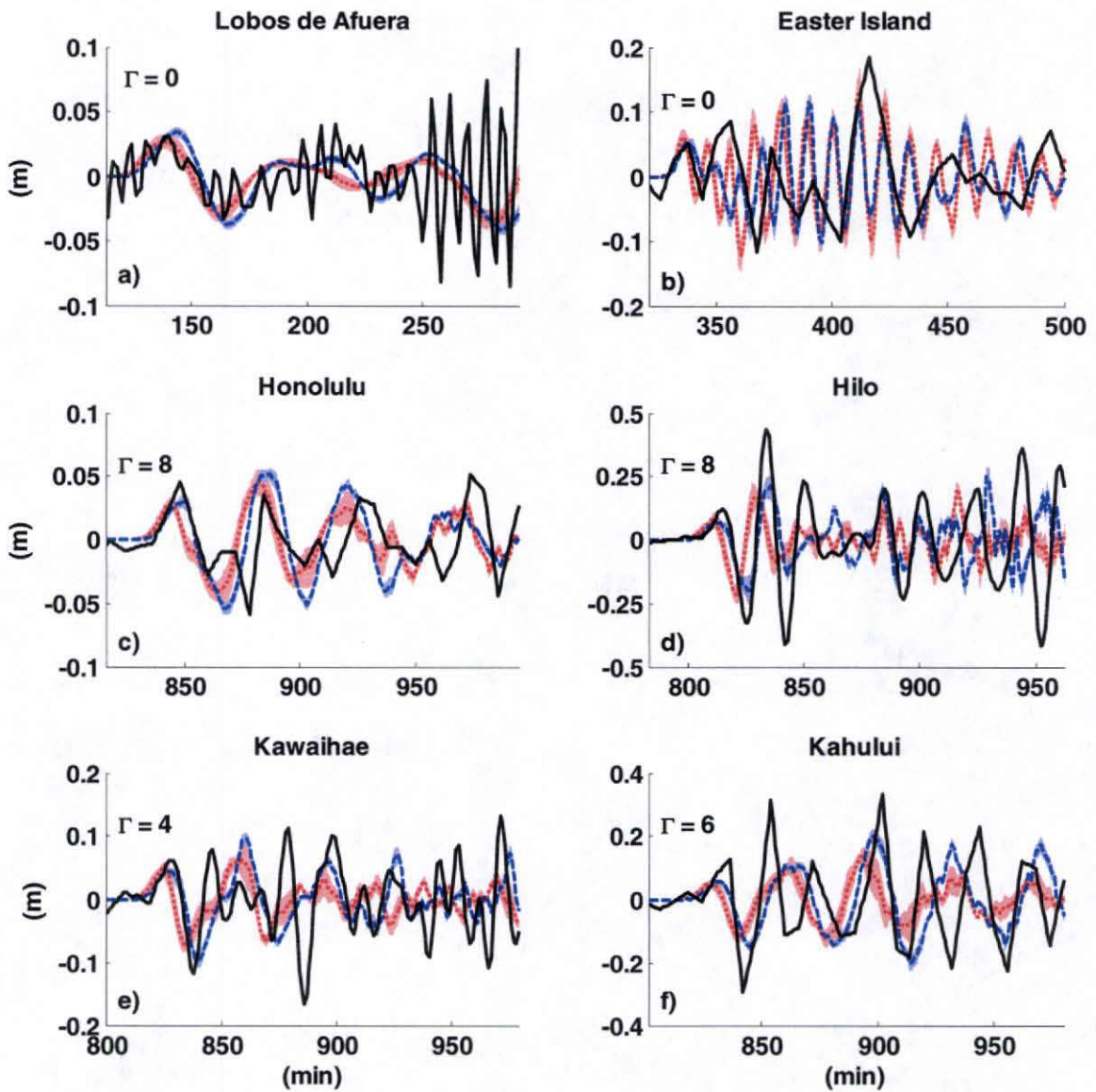


Figure 16. Computed and recorded waveforms at far-field tide gauges for the 2001 Atico-Peru tsunami.  $\Gamma$  indicates time shifts of computed waveforms to adjust for arrival times. ....., CIM; - - - -, AIM; , 95% confidence interval for CIM; , 95% confidence interval for AIM.

## REFERENCES

- Abe, K. (1972). Mechanisms and tectonic implications of the 1966 and 1970 Peru Earthquakes. *Physics of the Earth and Planetary Interiors*, 5, 367-379.
- Abe, K. and Noguchi, S. (1983). Revision of magnitudes of large shallow earthquakes. 1897-1912. *Physics of Earth and Planetary Interiors*, 33(1), 1-11.
- Ammon, C.J, Ji, C., Thio, H.K., Robinson, D., Ni, S., Hjorleifsdottir, V., Kanamori, H., Lay, T., Das, S., Helmberger, D., Ichinose, G., Polet, J. and Wald, D. (2005). Rupture Process of the 2004 Sumatra-Andaman Earthquake. *Science*, 308(5725), 1133-1139
- Araujo, M. and Suárez G. (1994). Geometry and state of stress of the subducted Nazca Plate beneath central Chile and Argentina: evidence from teleseismic data. *Geophysical Journal International*, 116(2), 283-303.
- Barazangi, M. and Isacks, B.L. (1976). Spatial distribution of earthquakes and subduction of the Nazca plate beneath South America. *Geology*, 4(11), 686-692.
- Barrietos, S. E. and Ward S. N. (1990). The 1960 Chile earthquake: inversion for slip distribution from surface deformation. *Geophysical Journal International*, 103, 589-598.
- Beck, S. and Ruff L. (1989). Great earthquake and subduction along the Peru trench. *Physics of the Earth and Planetary Interiors*, 57(3-4), 199-224.
- Beck, S., Barrietos, S., Kausel, E. and Reyes M. (1998). Source Characteristics of historical earthquakes along the Central Chile subduction zone. *Journal of South American Earth Sciences*, 11(2), 115-129.
- Benioff, H. Press, F. and Smith, S.W. (1961). Excitation of the free oscillations of the earth by earthquakes. *Journal of Geophysical Research*, 66(2), 605-619
- Berninghausen, W.H. (1962). Tsunami reported from the West Coast of South America 1562-1960. *Bulletin of the Seismological Society of America*, 52(4), 915-921.
- Bohm, M., Lüth, S., Echtler, H., Asch, G. Bataille, K., Bruhn, C., Rietbrock, A. and Wigger, P. (2002). The Southern Andes between 36° and 40°S latitude: seismicity and average seismic velocities. *Tectonophysics*, 356(4), 275-289.
- Carlo, L.D., Lay, T., Ammon, C.J. and Zhang J. (1999). Rupture process of the 1995 Antofagasta subduction earthquake. *Pure and Applied Geophysics*, 154(3-4), 677-709.
- Chleih M., de Chabaliér, J.B., Ruegg, J.C., Armijo, R., Dmowska, R., J. Campos and Feigl K.L. (2004). Crustal deformation and fault slip during the seismic cycle in the North Chile subduction zone, from GPS and InSAR observations. *Geophysical Journal International*, 158(11), 695-711.
- Choy G.L. and Kirby S.H. (2004). Apparent stress, fault maturity and seismic hazard for normal-fault earthquakes at subduction zones. *Geophysical Journal International*, 159(8), 991-1012.

- Cifuentes, I. (1989). The 1960 Chilean earthquakes. *Journal of Geophysical Research*, 94(B1), 665-680.
- Cifuentes, I. and Silver, P. (1989). Low frequency source characteristics of the great 1960 Chilean earthquake. *Journal of Geophysical Research*, 94(B1), 923-934
- Comte, D. and Pardo, M. (1991). Reappraisal of great historical earthquakes in the northern Chile and Southern Peru seismic gaps. *Natural Hazards*, 4(1), 23-44.
- Comte, D. and Suárez, G. (1995). Stress distribution and geometry of the subducting Nazca plate in Northern Chile using teleseismically recorded earthquakes. *Geophysical Journal International*, 122(2), 419-440.
- Comte, D., Dorbath, L., Pardo, M., Monfret, T., Haessler H, Rivera, L., Michel, F., Glass, B. and Meneses, C. (1999). A doubled-layered seismic zone in Arica, Northern Chile. *Geophysical Research Letters*, 26(13), 1965-1968.
- Comte, D., Haessler, H., Dorbath, L., Pardo, M., Monfret, T., Lavenu, A., Pontoise, B. and Hello, Y. (2002) Seismicity and stress distribution in the Copiapo, Northern Chile subduction zone using combined on- and off-shore seismic observations. *Physics of Earth and Planetary Interiors*, 132(1), 197-217.
- Delouis, B., Cisternas, A., Dorbath, L., Rivera, L. and Kausel E. (1996). The Andean subduction zone between 22 and 25°S (Northern Chile): precise geometry and state of stress. *Tectonophysics*, 259(1-3), 81-100.
- Delouis, B., Monfret, T., Dorbath, L., Pardo, M., Rivera, L., Comte, D., Haessler, H., Caminade, J.P., Ponce, L., Kausel, E. and Cisternas, A. (1997). The Mw = 8.0 Antofagasta (Northern Chile) earthquake of 30 July 1995: a precursor to the end of the large 1877 gap. *Bulletin of the Seismological Society of America*, 87(2), 427-445.
- DeMets, C.R., Gordon, R.G., Argus, D., Stein, S. (1990). Current plate motion. *Geophysical Journal International*, 101, 425-478.
- DeMets, C.R., Gordon, R.G., Argus, D. and Stein, S. (1994). Effect of recent revisions to the geomagnetic reversal time scale on estimates of current plate motions. *Geophysical Research Letters*, 21(20), 2191-2194.
- Dewey, J.W., and Spence, W. (1979). Seismic gaps and source zones of recent large earthquakes in coastal Peru. *Pure and Applied Geophysics*, 117(6), 1148-1171.
- Duda, S.J. (1963). Strain release in the circum-Pacific belt, Chile, 1960. *Journal of Geophysical Research*, 68, 5531-5544.
- Dorbath, L., Cisternas, A. and Dorbath, C. (1990). Quantitative assessment of great earthquakes in Peru. *Bulletin of the Seismological Society of America*, 80(3), 551-576.
- Eble, M.C. and González, F.I. (1991). Deep-ocean bottom pressure measurements in the Northeastern Pacific. *Journal of Atmospheric Ocean Technology*, 8(2), 221-233.
- Efron, B. (1982). The jackknife, the bootstrap and other resampling plans. Lecture notes series, *Society of Industrial and Applied Mathematics*, Philadelphia.
- Fisher, R.L. and Raitt, R.W. (1962). Topography and structure of the Peru-Chile trench. *Deep Sea Research*, Part I, 9, 423-443.

- GEBCO (2003). The General Bathymetric Chart of the Oceans – 1-minute Global Digital Atlas Centenary Edition, CD-ROM, British Oceanographic Data Centre Birkenhead, England
- Giovanni, M.K., Beck S.L. and Wagner L. (2002). The June 23, 2001 Peru earthquake and the southern Peru subduction zone. *Geophysical Research Letters*, 29(21), 2018-2032
- Gica, E., Spillane, M., Titov, V.V. and Chamberlin C. (2006). Development of the forecast propagation database for the NOAA Tsunami Forecasting System. NOAA Tech. Memo, OAR PMEL-131.
- Hasegawa, A., and Sacks, I.S. (1981). Subduction of the Nazca plate beneath Peru as determined from seismic observations. *Journal of Geophysical Research*, 86(B6), 4971-4980.
- Hank, T.C. and Kanamori H. (1979). A moment-magnitude scale. *Journal of Geophysical Research*, 84, 2348-2350.
- Herron, E.M. (1981). Chile margin near 38°S: Evidence for a genetic relationship between continental and marine geologic features or a case of curious coincidences?, Nazca Plate: Crustal formation and Andean convergence. *Geological Society of America, Memoir*, 154, 755-760.
- Hino, R., Tanioka, Y., Kanazawa, T., Sakai, S., Nishino, M. and Suyehiro, K. (2001). Micro-tsunami from a local interpolate earthquake detected by cabled offshore tsunami observation in Northeastern Japan. *Geophysical Research Letters*, 28(18), 3533-3536.
- Hyndman, R.D. and Wang, K. (1993). Thermal constraints of the zone of major thrust earthquake failure: The Cascadia subduction zone. *Journal of Geophysical Research*, 98(B2), 2039-2060.
- Isacks, B. and Molnar, P. (1971). Distribution of stresses in the descending lithosphere from a global survey of focal mechanism solutions of mantle earthquakes. *Reviews of Geophysics and Space Physics*, 9, 103-174.
- Johnson, J.M. (1999). Heterogeneous coupling along Alaska-Aleutians as inferred from tsunami, seismic, and geodetic inversion. *Advances in Geophysics*, 39, 1-110.
- Kanamori, H. and Cipar J. (1974). Focal process of the great Chilean Earthquake of May 22, 1960. *Physics of the Earth and Planetary Interiors*, 9(\*), 128-136.
- Kanamori, H. (1977). The energy release in great earthquakes. *Journal of Geophysical Research*, 82(20), 2981-2987.
- Kelleher, J.A. (1972). Rupture zones of large South American earthquakes and some predictions. *Journal of Geophysical Research*, 77(\*), 2089-2103.
- Kikuchi, M. and Yamanaka, Y. (2001). Near coast of Peru earthquake ( $M_w$  8.2) on June 23, 2001, Earthquake Information Center Seismological Note 105, Web address: [http://www.eic.eri.u-tokyo.ac.jp/EIC/EIC\\_News/105E.html](http://www.eic.eri.u-tokyo.ac.jp/EIC/EIC_News/105E.html)

- Liu, P.L.-F., Cho, Y.-S., Briggs, M.J., Kanoglu, U. and Synolakis, C.E. (1995). Runup of solitary waves on a circular island. *Journal of Fluid Mechanics*, 302, 259-285.
- Lockridge, P.A. (1985). Tsunamis in Peru-Chile, World Data Center-A for Solid Earth Geophysics, Report SE-39, National Geophysical Data Center, National Oceanographic and Atmospheric Administration, Boulder Colorado, U.S.A., pp. 97
- Lomnitz, C. (1970). Major earthquakes and tsunamis in Chile during the period 1535-1955. *Geologische Rundschau*, 59(\*), 938-960.
- Lüth, S., Wigger, P. and the ISSA Research Group (2003). A crustal model along 39°S from a seismic refraction profile- ISSA 2000. *Revista Geologica de Chile*, 30(1), 83-101.
- McCann, W.R., Nishenko, S.P., Sykes, L.R. and Krause, J. (1979). Seismic gaps and plate tectonics: Seismic potential for major boundaries. *Pure and Applied Geophysics*, 117(\*), 1082-1147.
- Okal, E.A. (1992). Use of mantle magnitude  $M_m$  for the reassessment of the moment of historical earthquakes I: Shallow events. *Pure and Applied Geophysics*, 139, 17-57.
- Okada, Y. (1985). Surface deformation due to shear and tensile faults in a half space. *Bulletin of the Seismological Society of America*, 75(4), 1135-1154.
- Oleskevich, D.A., Hyndman, R.D. and Wang, K. (1999). The updip and downdip limits to great subduction earthquakes: Thermal and structural models of Cascadia, south Alaska, SW Japan, and Chile. *Journal of Geophysical Research*, 104(B7), 14965-14991.
- Pardo, M., Comte, D., Monfret, T., Boroschek, R. and Astroza, M. (2002a). The October 15, 1997 Puntiaqui Earthquake (Mw 7.1): A destructive event within the subducting Nazca Plate in Central Chile. *Tectonophysics*, 345(\*), 199-210.
- Pardo, M., Comte, D. and Monfret T. (2002b). Seismotectonic and stress distribution in the Central Chile subduction zone. *Journal of South American Earth Sciences*, 15(\*), 11-22.
- Plafker, G. and Savage J.C. (1970). Mechanism of the Chilean earthquakes of May 21 and 22, 1960. *Geological Society of America*, 81(\*), 1001-1030.
- Plafker, G. (1972). Alaskan earthquake and Chilean earthquake of 1960: Implications for arc tectonics. *Journal of Geophysical Research*, 77(\*), 901-925.
- Powell, M.J.D. (1978). A Fast Algorithm for Nonlinearly Constrained Optimization Calculations, Numerical Analysis. Ed. G.A. Watson, Lecture Notes in Mathematics, Springer Verlag, Vol. 630, where published?
- Ruegg, J. C., Campos, J., Armijo, R., Barrientos, S., Briole, P., Thiele, R., Arancibia, M., Cañuta, J., Duquesnoy, T., Chang, M., Lazo, D., Lyon-Caen, H., Ortlieb, L., Rossignol, J.C. and Serrurier, L. (1996). The  $M_w=8.1$  Antofagasta (North Chile) earthquake of July 30, 1995: first results from teleseismic and geodetic data. *Geophysical Research Letters*, 23(9), 917-920.

- Ruegg, J.C, Oclay, M., Chabalier, J.B. and Lazo, D. (2002). Coseismic and aseismic slip observed from continuous GPS measurements for the 2001 Southern Peru earthquake. *International Symposium of Andean Geodynamics*, City, State or Country.
- Satake, K. (1987). Inversion of tsunami waveforms for the estimation of a fault heterogeneity: method and numerical experiments. *Journal of Physics of the Earth*, 35(3), 241-254.
- Satake, K. (1989). Inversion of tsunami waveforms for the estimation of heterogeneous fault motion of large submarine earthquakes: The 1968 Tokachi-oki and the 1983 Japan Sea earthquake. *Journal of Geophysical Research*, 94(\*), 5627-5636.
- Satake, K. and Tanioka Y. (1999). Sources of tsunami and tsunamigenic earthquakes in subduction zones. *Pure and Applied Geophysics*, 154(\*), 467-483.
- Seno, T. and Yoshida, M. (2004). Where and why do large shallow intraslab earthquakes occur. *Physics of Earth and Planetary Interiors*, 141(\*), 183-206.
- Soloviev, S.L., and Go, C.N. (1975). Catalogue of tsunamis of the eastern shore of the Pacific Ocean. *Nauka Publishing House*, Moscow, pp. 204. (in Russian; English translation: Canadian Translation. (1984). *Fisheries and Aquatic Science*, No. 5078, Ottawa, pp. 293.)
- Song, Y.T., Ji, C., Fu, L.L., Zlotnicki, V., Shum, C.K., Yi, Y. and Hjorleifsdottir, V. (2005). The 26 December 2004 tsunami source estimated from satellite radar altimetry and seismic waves. *Geophysical Research Letters*, 32(1), 1-5.
- Stauder, W. (1973). Mechanism and spatial distribution of Chilean earthquakes with relation to the oceanic plate. *Journal of Geophysical Research*, 78(\*), 5033-5061.
- Stauder, W. (1975). Subduction of the Nazca Plate under Peru as evidenced by focal mechanisms and by seismicity. *Journal of Geophysical Research*, 80(8), 1053-1064.
- Steketee, J.A. (1958). On Volterra's dislocations in a semi-infinite elastic medium. *Canadian Journal of Physics*, 36(\*), 192-205.
- Swenson, J. and Beck, S.L. (1996). Source characteristics for the 1942 Ecuador and 1942 Peru subduction zone earthquakes. *Pure and Applied Geophysics*, 146(\*), 67-102
- Swenson, J. L. and Beck S.L. (1999). Source characteristics of the 12 November 1996 Mw 7.7 Peru Subduction earthquake. *Pure and Applied Geophysics*, 154(\*), 731-751.
- Swift, S. and Carr M. (1974). The Segmented Nature of the Chilean Seismic Zone. *Physics of Earth and Planetary Interiors*, 9(\*), 183-191.
- Symons, J.M. and Zetler B.D. (1962). The tsunami of May 22, 1960 as recorded at tide stations; preliminary report, Washington, U.S. Department of Commerce, Coast and Geodetic Survey, City, State.
- Tichelaar, B.E. and Ruff, L.J. (1989). How good are our best models? Jackknifing, bootstrapping, and earthquake depth. *EOS Transactions American Geophysical Union*, 70(20), 597-606.
- Tichelaar, B.E. and Ruff, L.J. (1991). Seismic coupling along the Chilean subduction zone. *Journal of Geophysical Research*, 96(B7), 11997-12022.

- Titov, V.V., Mofjeld, H.O., González, F.I. and Newman, J.C. (1999). Offshore Forecast of Hawaiian Tsunamis Generated in Alaskan-Aleutian Subduction Zone. *Technical Memorandum ERL PMEL-114*, National Oceanic and Atmospheric Administration, Seattle, Washington.
- Titov, V.V., González, F.I., Bernard, E.N., Eble, M.C., Mofjeld, H.O., Newman, J.C. and Venturato, A.J. (2005). Real-time tsunami forecasting: Challenges and solutions. *Natural Hazards*, 35(1), 41-58.
- Tsang, E. (1995). Foundations of Constraint Satisfaction, *Academic Press Limited*, London, pp. 421
- Walker, D.A. (2004). Regional tsunami evacuations for the State of Hawai'i: A feasibility study based on historical runup data. *Science of Tsunami Hazards*, 22(1), 3-16
- Wells, D.L. and Coppersmith, K.J. (1994). New empirical relationships among magnitude, rupture length, rupture width, rupture area, and surface displacement. *Bulletin of the Seismological Society of America*, 84(4), 974-1002.
- Wei, Y., Cheung, K.F., Curtis, G.D. and McCreery, C.S. (2001). Tsunami heights forecast from water-level data, OCEANS 2001 MTS/IEEE Proceedings, Hawai'i, Vol. 4, pp. 2051-2058.
- Wei, Y., Cheung, K.F., Curtis, G.D. and McCreery, C.S. (2003). Inverse algorithm for tsunami forecast. *Journal of Waterway, Port, Coastal and Ocean Engineering*, 129(2), 60-69.
- Wei, Y. (2006). Tsunami Runup Model and Forecast. PhD Thesis, University of Hawaii, Honolulu, Hawaii.
- Wessel, P. and Smith W.H.F. (1991). Free software helps map and display data. *EOS Transcripts, American Geophysical Union*, 72(41), 441.
- Wu, C.F.J. (1986). Jackknife, bootstrap, and other resampling methods in regression analysis. *The Annals of Statistics*, 14(4), 1261-1295.
- Yamazaki, Y., Wei, Y., Cheung, K.F. and Curtis G.D. (2006). Forecast of tsunamis from the Japan-Kuril-Kamchatka source region. *Natural Hazards*, 38(3), 411-435.

## APPENDIX A

### SEAFLOOR DEFORMATION DUE TO FAULTING

The vertical surface deformation for a finite, dip-slip (reverse and reverse fault) and rectangular fault is given by (Okada, 1985)

$$u_z = -\frac{U_2}{2\pi} \left[ \frac{\tilde{d}q}{R(R+\psi)} + \sin(\delta) \tan^{-1} \left( \frac{\psi\phi}{qR} \right) - I_s \sin(2\delta) \right]$$

in which

$$f(\psi, \phi) = f(y, p) - f(y, p-W) - f(y-L, p) + f(x-L, p-W)$$

$$I_s = \frac{\mu}{\lambda + \mu} \frac{2}{\cos \delta} \tan^{-1} \left( \frac{\phi(X + q \cos \delta) + X(R + X) \sin \delta}{\psi(R + X) \cos \delta} \right)$$

$$p = x \cos \delta + d \sin \delta \quad q = x \sin \delta - d \cos \delta$$

$$\tilde{d} = \phi \sin \delta - q \cos \delta \quad R^2 = \psi^2 + \phi^2 + q^2$$

$$X^2 = \psi^2 + q^2$$

where  $\lambda$  is the rake,  $\delta$  is the dip and  $L$  and  $W$  are the length and width,  $\psi$  and  $\phi$  are the axes along the length and width of the fault,  $x$ ,  $y$  and  $p$  are the projected axes and  $d$  is the depth.

## APPENDIX B

### CORRELATION COEFFICIENT

The correlation coefficient between  $x$  and  $y$  is defined as

$$R = \frac{n \sum xy - \sum x \sum y}{\sqrt{(n \sum x^2 - (\sum x)^2)(n \sum y^2 - (\sum y)^2)}}$$

where  $n$  is the length of the record